Optics & Laser Technology 199 (2026) 114988

Contents lists available at ScienceDirect

Optics and Laser Technology

journal homepage: www.elsevier.com/locate/optlastec

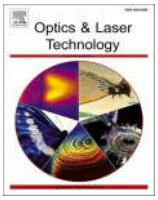

Full length article

Improving adhesion of hybrid Ti-CFRP joints obtained by direct co-bonding technique through laser surface treatments

Davide Morello [a], Genna Silvio [b,c], Claudio Leone [a,c,*]

[a] University of Campania Luigi Vanvitelli, Department of Engineering, via Roma 29, 81031 Aversa (CE), Italy
[b] University of Rome Tor Vergata, Department of Enterprise Engineering, via del Politecnico 1, 00133 Rome, Italy
[c] CIRTIBS Research Centre, University of Campania Luigi Vanvitelli, via Roma 29, 81031 Aversa (CE), Italy

ARTICLE INFO

Keywords:
Co-bonding
Hybrid joints
Laser texturing
Laser cleaning
CFRP
Titanium alloy

ABSTRACT

The paper focuses on the development of a laser-based surface treatment aimed at enhancing the adhesive strength of Ti6Al4V alloy-CFRP joints manufactured through direct co-bonding. To this end, the effect of process parameters on the groove geometry (depth, width, taper angle, and burr) that forms the texture was studied using ANalysis Of VAriance (ANOVA) and Response Surface Methodology (RSM). Two groove geometries were selected and adopted to produce two textures that differed in groove width and were similar in groove depth and filling factor. In addition to the two textures, a laser cleaning treatment was developed to treat the untextured area. Single lap joints were produced by adopting the two textures, both with and without laser cleaning treatment, and tested according to the ASTM Standards. The joints were obtained by direct co-bonding during the fabrication of CFRP through infusion techniques. Additionally, specimens subjected solely to laser cleaning and sandpaper abrasion were produced and designated as reference samples. Differences among the treatments with respect to strength and failure energy were evaluated using a one-way ANOVA and Tukey's method for multiple comparisons. Results show that, compared to the sandpaper treatment, the laser cleaning treatment increases joint strength and failure energy by approximately 3 and 20 times, respectively. By adopting laser texturing, strength and failure energy increased by up to 6.5-fold and 75-fold, reaching approximately 18 MPa and 23.17 J, respectively. These values are comparable to those observed for similar joints in the main bibliography.

1. Introduction

In recent years, the combination of titanium alloys with carbon fibre reinforced polymers (CFRPs) has garnered the attention of scholars and industry to develop new applications in several fields, such as aerospace, automotive, naval, sports equipment, etc. This material combination enables the exploitation of the strength, corrosion resistance, and superior fatigue performance of titanium alloys, alongside the high strength-to-weight ratio, stiffness, and resistance to environmental degradation offered by CFRP [1,2]. Traditionally, mechanical fastening and adhesive bonding have been adopted as joining methods: the first one provides strong joint strength and simplifies assembly, but it can damage CFRP and add weight. Conversely, adhesive bonding promotes a uniform stress distribution and offers several benefits, including weight reduction, shorter processing times, reduced corrosion, acoustic insulation, and vibration attenuation; however, it demands meticulous surface preparation and remains susceptible to environmental degradation [3–5]. The Ti-CFRP bonding is challenging due to their different mechanical, thermal, and chemical characteristics. To enhance joint strength, substrate surface treatments have been developed before bonding to control surface energy, roughness, and chemistry [6]. Mechanical methods, such as sanding, grinding and abrasive blasting, are commonly used as surface treatments to increase the surface roughness of the substrate before bonding. However, these treatments can entrap contaminants within the material and damage the component [7], and they require considerable time for masking and unmasking operations during preparation, as they do not allow precise control of the treated area. Moreover, the presence of powder raises significant concerns about its environmental impact and the associated disposal costs. It also poses risks to the health and safety of workers. Alternatively, the use of chemical methods has resulted in a marked improvement in adhesive bonding performance compared to mechanical approaches [8], high waste disposal costs, and health and safety concerns. Then, their application is restricted to the most critical cases.

* Corresponding author.
E-mail address: claudio.leone@unicampania.it (C. Leone).

https://doi.org/10.1016/j.optlastec.2026.114988
Received 29 May 2025; Received in revised form 4 December 2025; Accepted 13 February 2026
Available online 20 February 2026

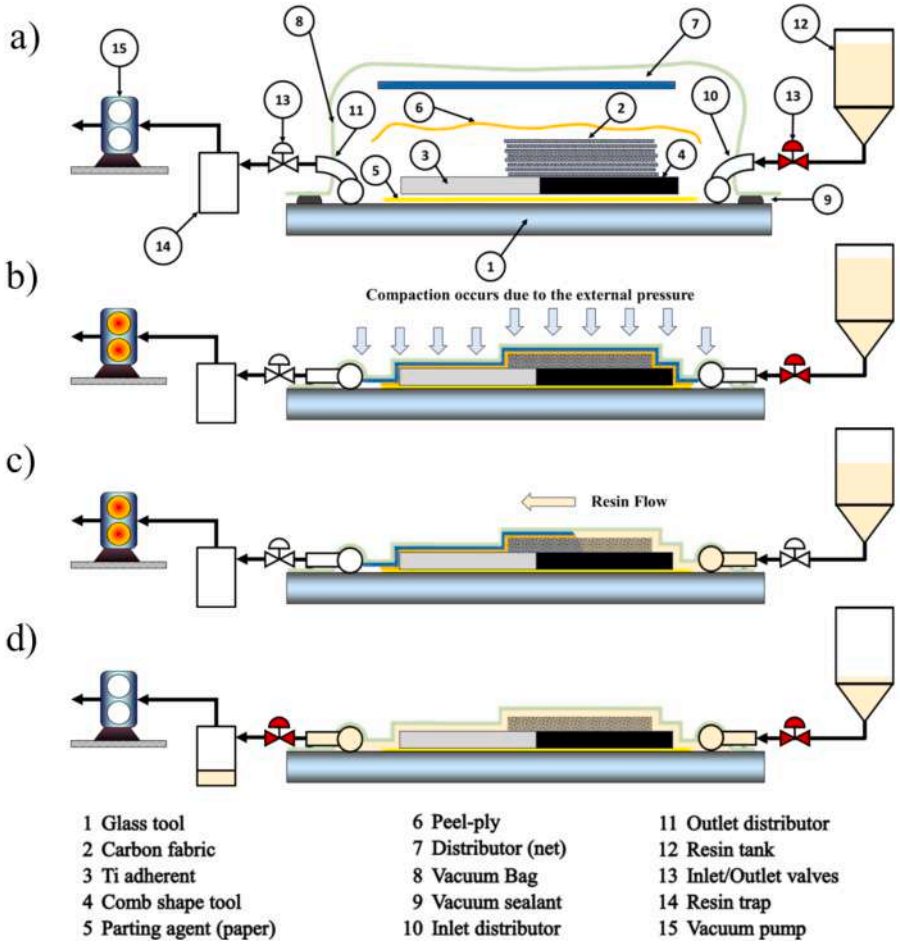

Fig. 1. Schematic of the infusion process: a) Die composition; b) Vacuum application; c) Resin infusion; d) Impregnation stop, valves closed, and vacuum pump turned off.

The adoption of laser texturing and laser cleaning processes emerged as a promising alternative to mechanical and chemical methods for the preliminary preparation of adhesive joints between homogeneous or non-homogeneous materials [8–10]. Laser texturing creates surface patterns (dimples, grooves, grids) to enhance mechanical interlocking [11,12]. The advantages of these techniques include contact-free processing, independence from material hardness, precise definition of the treated area, controllable material removal, reduced environmental impact, and enhanced worker safety. Laser cleaning comprises a family of surface treatments that adopt pulsed lasers (typically short or ultrashort lasers) to peel off, vaporise, sublimate, or burn away unwanted material without causing specific harm to the substrate. The process is used in several applications to remove unwanted surface materials, such as paints [13–15], rust [16,17], coatings [18], oil [19], or in surface preparation before welding [20], coating [21,22], and bonding [23,24]. Additionally, by adjusting the laser parameters, it is possible to generate micro- or nano-textured surfaces, providing better grip for adhesive areas, as well as frictional and mechanical anchoring. In [25], Laser-induced surface reconstruction (LISR) was applied to enhance adhesive bonding in CFRP/Ti alloy hybrid structures. In detail, both substrates were laser-treated, resulting in a cross-like surface texture (~14 μm depth) that did not damage the carbon fibres in the CFRP substrate, while increasing the wettability and surface roughness of both surfaces due to the formation of polar functional groups. Failure analysis revealed that laser ablation shifted the fracture location from the CFRP substrate to the carbon fibres, enabling fibre pull-out and additional energy dissipation, ultimately improving bonding performance. The effect of different surface textures (dots, grid and chaotic pattern) on the adhesion performance of laser-treated Ti6Al4V alloy was studied in [26]. The results showed that the adoption of laser treatment allows an increase in the joint's strength through the combination of mechanical interlocking, due to the increase in roughness, and chemical composition modification generated by the laser process. Indeed, the adoption of a grid texture or a chaotic pattern can shift the failure mode from adhesive to cohesive. Recently, the effect of laser texturing as a prior bonding treatment was also studied in the hot joining of titanium alloys (Ti6Al4V) and carbon fibre-reinforced polymer (CFRP). Studies have shown that laser-induced microstructures improved the wettability of molten CFRP on textured titanium surfaces, significantly enhancing joint strength. It was demonstrated that, compared to untreated surfaces, a grid-patterned texture increased shear force by up to 156%; furthermore, by selecting an appropriate texture depth, incomplete adhesive filling can be prevented [27,28]. Similarly, the texture orientation plays a crucial role; perpendicular grooves to the tensile direction yield a 111% increase in shear strength compared to a 42.9% increase for orthogonal ones [29].

Schmid et al. [30] propose a classification of adhesive bonding into three distinct types: i) Co-curing that involves curing all components simultaneously within a single manufacturing process (for instance, two or more composite pieces, with different characteristics); ii) Secondary bonding refers to the joining of two parts, that have already been cured/finished, typically using a film or paste adhesive; iii) Co-bonding follows an hybrid approach, an uncured component (i.e. composite) is joined to one or more cured/finished parts, either with an additional adhesive layer or without any adhesive during its curing process. When no adhesive is used, the process is referred to as direct co-bonding. An

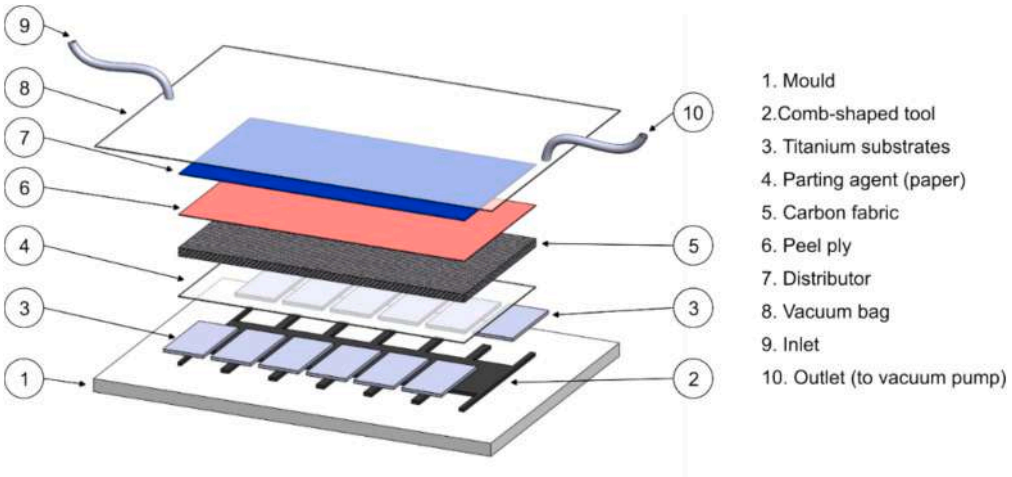

Fig. 2. Detail of the infusion system.

Table 1
Mechanical and physical properties of adopted materials.

Property	Units	Ti6Al4V	Fibre	I-SX 8*
Tensile strength	MPa	1170	4410	55 ÷ 65
Tensile Yield	MPa	1100	–	–
Tensile modulus	GPa	114	250	2.8 ÷ 3.3
Elongation	%	10	1.8	2 ÷ 3
Density	kg/m^3	4.43	1750	950
Thermal conductivity	Wm^{-1}K^{-1}	6.70	50	n.a.
Specific heat	Jkg^{-1}K^{-1}	0.5263	700	n.a.
Tg, Dry (Tg, Wet)	°C	–	–	89**
Pot life	Min	–	–	45–60
Gel time	h	–	–	5–6
Viscosity (at 20°C)	mPas	–	–	550–880

*After 7 days at 25°C,
** Max values.

example of direct co-bonding is the joining of two or more composite pieces, where at least one has been previously cured [31] or the insertion of a metal component (insert) into the laminate during the manufacturing of the composite, thereby adopting the matrix as an adhesive. Although the absence of the adhesives may involve different advantages, such as a reduction of the process phase and process times, the stress distribution improving by embedding the component inside the CFRP, reduction of required materials (i.e. the adhesive), warehouse stock, and problems in managing their expiration date; since the polymer is designed to act as a matrix rather than an adhesive, it should not be assumed that it will perform equally well in an adhesive role.

Then, to enhance the joint strength in a direct co-bonding operation, it is essential to require the contribution of the fibre strength to the joining. Despite the drawback mentioned above, the bibliography indicates that laser treatment can enhance adhesive bonding. At the same time, studies on the use of laser treatments in direct co-bonding operations for hybrid joints are lacking in the literature.

The present study focuses on the development of a laser-based surface treatment aimed at enhancing the adhesive strength of Ti6Al4V alloy-CFRP joints manufactured through direct co-bonding. Moreover, it would demonstrate that, with an appropriate laser treatment, direct co-bonding techniques can achieve joint strength comparable to that reported for similar joints in the main bibliography [1,4,7]. Then, in the first part of the work, an in-depth analysis of the laser texturing process for Ti6Al4V alloy was conducted to determine the optimal treatment parameters. In detail, linear grooves were generated under different process conditions and characterised in terms of depth, width, taper angle, and burr. Analysis of Variance (ANOVA) and Response Surface Methodology (RSM) were adopted to develop a statistical model for estimating the groove geometry. Two groove configurations, differing in width but similar in depth and filling factor, were selected for the texture production. Furthermore, since in a previous study [32] it was found that the adoption of a laser cleaning treatment, in addition to the laser texturing, improves the joint's strength, a laser cleaning treatment was developed and applied either before or after the surface texturing. In the second part of the paper, Single-lap joints were subsequently fabricated through direct co-bonding techniques, after laser texturing, laser

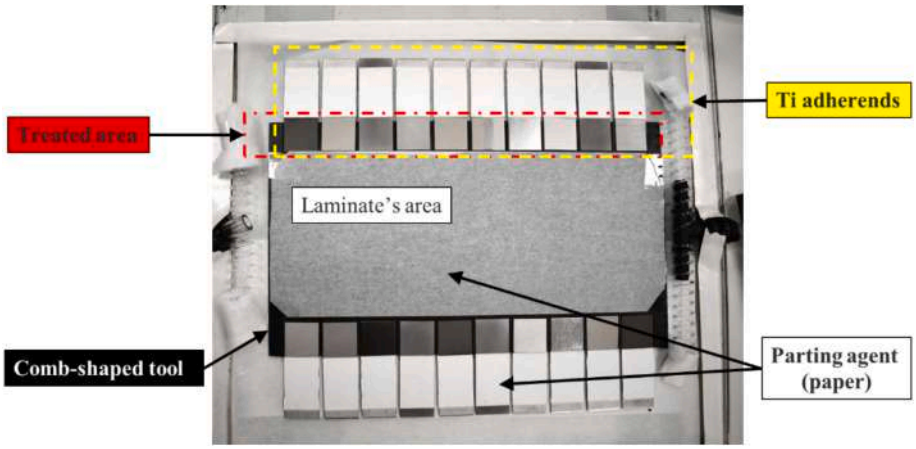

Fig. 3. Images of the titanium adherents arranged in the comb-shaped mould before the CFRP panel fabrication.

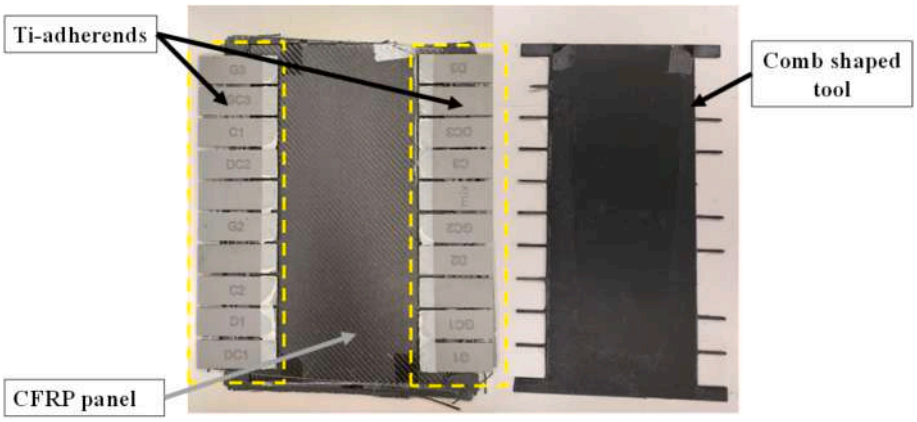

Fig. 4. Images of the components after demoulding.

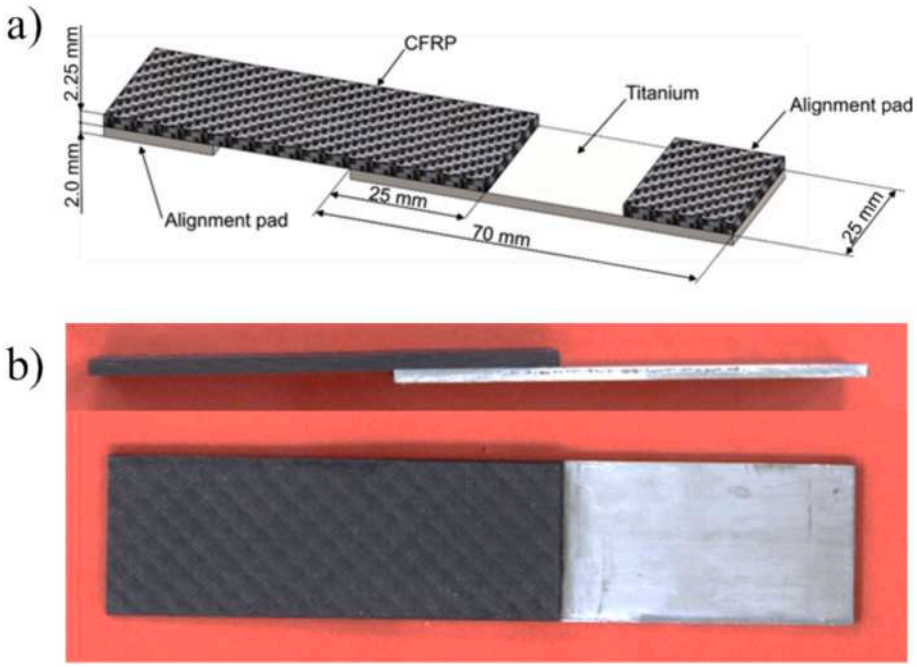

Fig. 5. Single lap joint: a) geometry and dimensions; b) Image.

Table 2
Laser systems characteristics.

Characteristic	Symbol	Unit	Value
Source	–		Yb:YAG
Wavelength	λ	nm	1064
Nominal average power	Pa	W	30
Pulse frequency	f	kHz	30 ÷ 80
Pulse duration	D	ns	50
Maximum pulse power	Pp	kW	20[a]
Maximum pulse energy	Pe	mJ	1[a]
Maximum scan speed	Ss	mm/s	5000
Mode	TEM	–	00
	M^2	–	1.2 ÷ 1.5
Focused spot diameter	–	μm	80

[a]At Pm = 30 W and F = 30 kHz

Table 3
Factors and levels adopted in the texture development.

Factor	Level	Values −2	−1	0	+1	+2
L	4	2	4	–	6	8
R	5	20	40	60	80	100

cleaning, and their respective combinations. The joints were tested according to ASTM Standards. Comparative analyses, including one-factor ANOVA and Tukey's multiple comparison method, were carried out to assess joint strength and failure energy across different surface treatments. Findings reveal that laser-treated co-bonded joints can achieve mechanical performance comparable to that obtained by adopting traditional adhesive joining techniques.

2. Materials, Equipment, and experimental procedures

2.1. Materials

Titanium Grade 5 (Ti6Al4V alloy) and CFRP laminate were adopted to produce single lap joints, according to the D5573-99, D5868-01, and D1002-10 ASTM Standards [33–35]. Samples of 25 × 70 mm^2 and 2 mm in thickness were obtained by diamond saw cutting of Ti alloy sheets;

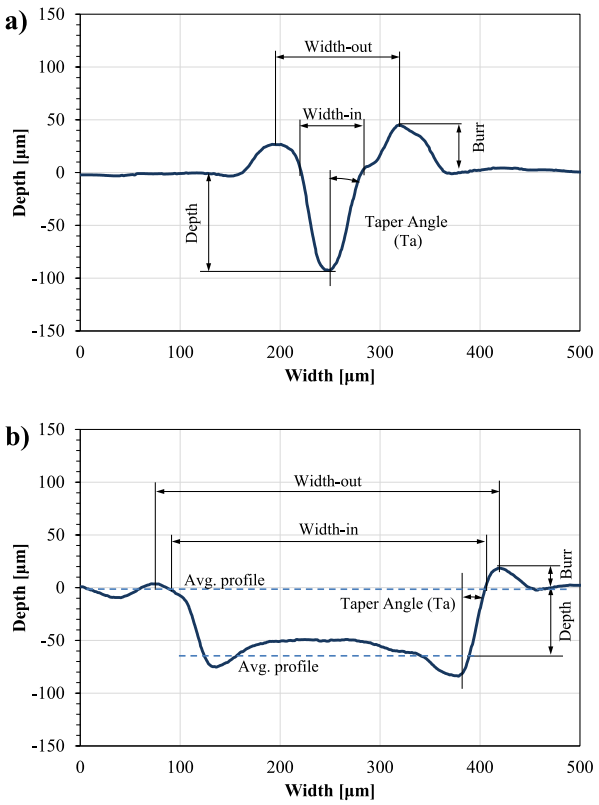

Fig. 6. Schematic of the groove section and the geometrical characteristics for profiles obtained at: a) R = 100 and L = 2; b) R = 100 and L = 8.

surfaces of 25 × 20 mm^2 were laser-treated according to the procedures reported in Paragraph 2.3. Immediately after the treatment, single lap joints were fabricated using direct co-bonding techniques, in accordance with the procedure outlined in [31]. A schematic of the process is reported in Fig. 1. The process involved the superposition of dry carbon fibres on the Ti adherents into a mould (here, a glass plate) which is sealed with a polymer film (vacuum bag), Fig. 1a. Then the vacuum is applied (−950 mbar) to evacuate air and compact the fibres against the Ti adherents, Fig. 1b. After that, the resin is introduced into the mould under vacuum pressure, between the vacuum bag and the reinforce, through a porous polymer net (the distributor). The latter allows the matrix to flow quickly into the fibres and fully saturate them, Fig. 1c. After complete impregnation, the inlet and the outlet are close, and the resin is left to cure at room temperature under vacuum, Fig. 1d. During the manufacturing process, a special comb-shaped tool, 2 mm in thickness, made in thermoplastic polymer was used to maintain the alignment of the Ti-adherents, ensure the correct positioning of the laminate, and prevent any possible movement of the components. Moreover, to prevent the adhesion of the matrix on specific parts of the system, pieces of parting agent (a release film) were placed in the critical points. In Fig. 2, a close-up view of the components' arrangement is reported.

The laminate was produced by adopting 8 dry plies of T400 carbon fabric 200 g/m^2, with 50% fibres in the warp and weft directions. A Becor I-SX8 epoxy matrix + Becor SX8-M hardener was adopted as the matrix. This resin system features a low viscosity (550–880 mPas) and a long pot life (45–60 min), making it suitable for infusion processes. Table 1 shows the properties of the adopted materials. Fig. 3 shows the titanium adherents arranged in the comb-shaped tool before the infusion process, while Fig. 4 shows a panel, after demoulding, and the comb-shaped tool. Once the panel was obtained, the samples were carefully separated by a diamond-tip water-cooled saw blade to avoid mechanical or thermal damage. The final thickness of the CFRP laminate was 2.25 ± 0.1 mm, whereas the adherent superposition was 25 mm. Fig. 5 shows the geometry and an image of the adopted single lap joint.

2.2. Laser Equipment

For the surface treatments, a Q-switched Yb:YAG fiber laser source (IPG, YLP-RA 30–1-50–20-20), working at the wavelength of λ = 1064

Table 4
Process conditions for the treatments adopted in the single lap.

Treatment	Texture type	Pre-treatment	Post-treatment	L	R	FF%
TX1	Texture 1	No	No	2	60	50
CTX1	Texture 1	Cleaning	No	2	60	50 + 100
TX1C	Texture1	No	Cleaning	2	60	50 + 100
TX2	Texture 2	No	No	8	60	50
CTX2	Texture 2	Cleaning	No	8	60	50 + 100
TX2C	Texture 2	No	Cleaning	8	60	50 + 100
C	Cleaning	No	No	n. a.	n. a.	100
SP	Sandpaper	No	No	n. a.	n. a.	100

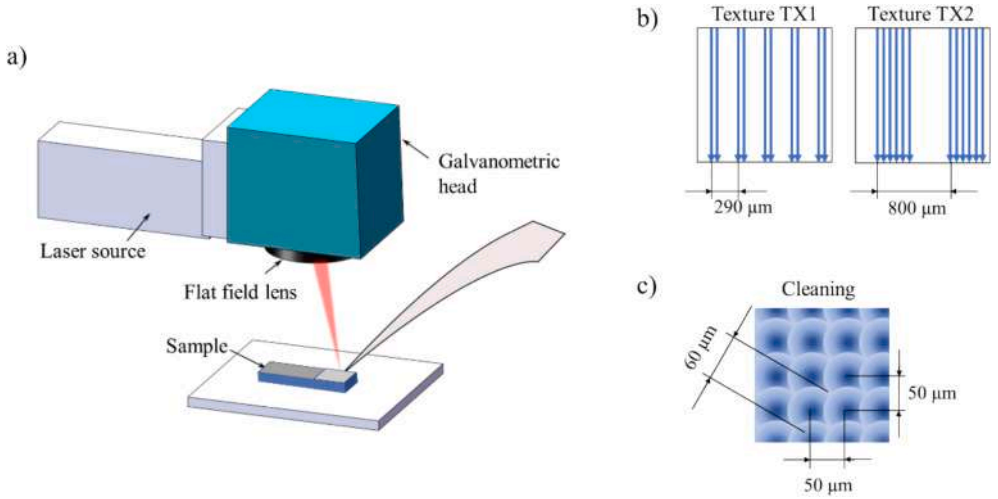

Fig. 7. Schematic of the surface treatments: a) Laser process; b) Texture pattern; c) Cleaning pattern.

Table 5
Summary of ANOVA table for RSM model.

Response variable	Source	Adj SS	Adj MS	F-Value	p-Value
Depth	L	2384.6	2384.6	57.76	**0.000**
	R	18537.4	18537.4	449.01	**0.000**
	L × L	388.4	388.4	9.41	**0.003**
	R × R	29.9	29.9	0.72	0.398
	L × R	56.9	56.9	1.38	0.245
	R-sq [%]	90.56			
	R-sq(adj) [%]	89.69			
	R-sq(pred) [%]	88.20			
Width_out	L	504,421	504,421	3330.17	**0.000**
	R	1729	1729	11.42	**0.001**
	L × L	23	23	0.15	0.696
	R × R	437	437	2.89	0.095
	L × R	106	106	0.70	0.406
	R-sq [%]	98.41			
	R-sq(adj) [%]	98.26			
	R-sq(pred) [%]	97.98			
Width_in	L	530,885	530,885	3070.58	**0.000**
	R	733	733	4.24	**0.044**
	L × L	151	151	0.87	0.354
	R × R	1849	1849	10.69	**0.002**
	L × R	14	14	0.08	0.778
	R-sq [%]	98.28			
	R-sq(adj) [%]	98.12			
	R-sq(pred) [%]	97.87			
Burr	L	2547.1	2547.07	54.40	**0.000**
	R	4588.8	4588.78	98.01	**0.000**
	L × L	9.8	9.79	0.21	0.649
	R × R	2731.7	2731.70	58.35	0.000
	L × R	243.3	243.26	5.20	**0.027**
	R-sq [%]	80.01			
	R-sq(adj) [%]	78.16			
	R-sq(pred) [%]	75.73			
Taper angle	L	1789.7	1789.7	8.59	**0.005**
	R	16810.4	16810.4	80.64	**0.000**
	L × L	458.9	458.9	2.20	0.144
	R × R	26.8	26.8	0.13	0.721
	L × R	5.3	5.3	0.03	0.874
	R-sq [%]	62.91			
	R-sq(adj) [%]	59.47			
	R-sq(pred) [%]	54.58			

Table 6
Regression Equations in Uncoded Units.

Response variable	Equation	
Depth [μm] =	8.26 L + 0.825 R + 0.636 L × L − 0.00105 R × R − 0.0154 L × R	2)
Width_out [μm] =	63.6 + 41.30 L + 0.189 R − 0.156 L × L − 0.00403 R × R + 0.0210 L × R	3)
Width_in [μm] =	−11.9 + 38.56 L + 0.910 R + 0.397 L × L − 0.00829 R × R − 0.0076 L × R	4)

nm, was adopted. The laser source was equipped with a scanner head (from LASIT) and a 160 mm focal length flat-field lens, yielding a beam spot diameter of about 80 μm. This laser source features excellent absorption for all metals, the possibility to deliver the maximum power (30 W) across all frequencies, high pulse power and pulse energy (up to 20 kW and 1 mJ, respectively), and low power consumption (160 W). The latter characteristic is especially significant when considering environment and process sustainability, as discussed in [36–38]. Table 2 summarises the main characteristics of the laser system.

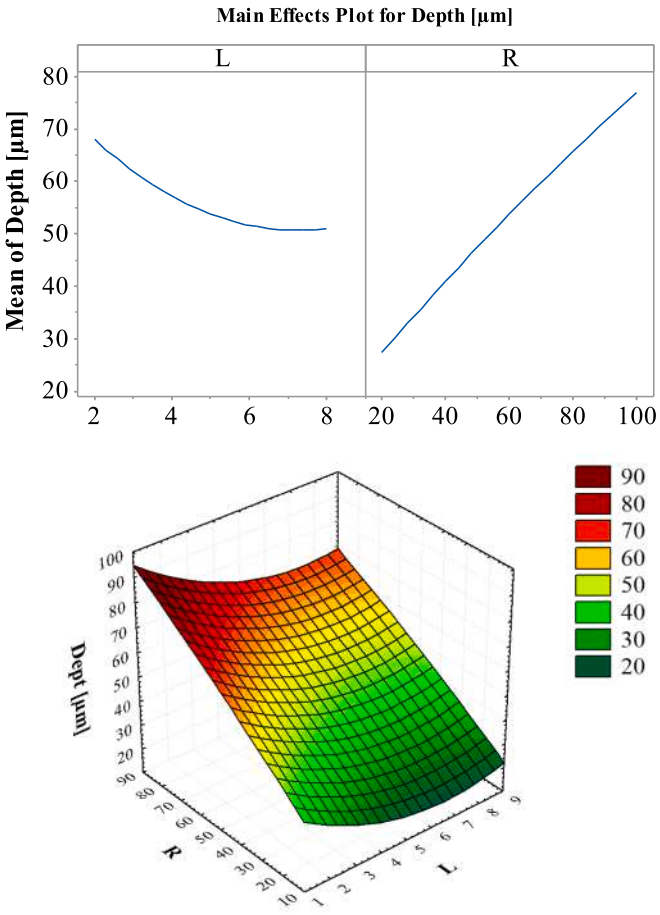

Fig. 8. Main effect plot and response surface for Depth.

2.3. Experimental Procedures

Before selecting the surface treatment, the laser texturing process of the Ti alloy was thoroughly investigated. This phase was essential for defining the process conditions to be adopted in the texturing treatment. Grooves of varying widths and depths were produced and geometrically characterised through 3D Digital microscopy (Hirox KH-8700). During the tests, the laser power (Pa), the pulse frequency (f) and the scanning speed (Ss) were fixed at 30 W, 30 kHz, and 300 mm/s, respectively, while the number of lines (L) and the scanning repetition (R) were adopted as control factor (i.e. the process parameters) to vary the width and the depth of the grooves. The fixed values were selected based on the previous experience [32,39–41] and preliminary tests. For L and R, a 4 × 5 full factorial design was developed and tested. Table 3 shows the R and L values adopted for the groove characterisation. At least five distinct profiles were recorded for each process condition. On each profile, the depth (Depth), the peak-to-peak width (Width_out), the internal width (Width_in), the burr eight (Burr) and the taper angle (Ta) were measured as shown in Fig. 6 and adopted as response variables. Analysis Of Variance (ANOVA), main effect plots analysis, and Response Surface Methodology (RSM) were employed to determine which process parameters affect the groove geometry and to model the grooving process. The analysis was conducted with a confidence level of 95% ($\alpha = 0.05$). Consequently, a control factor or an interaction is considered statistically significant if the *p*-value is less than 0.05. Since the ANOVA assumes that experiments are independent and normally distributed with equal variances between cutting conditions, the latter assumptions were successfully verified through residual analysis, as suggested in [42,43]; however, this analysis is not reported for the sake of brevity.

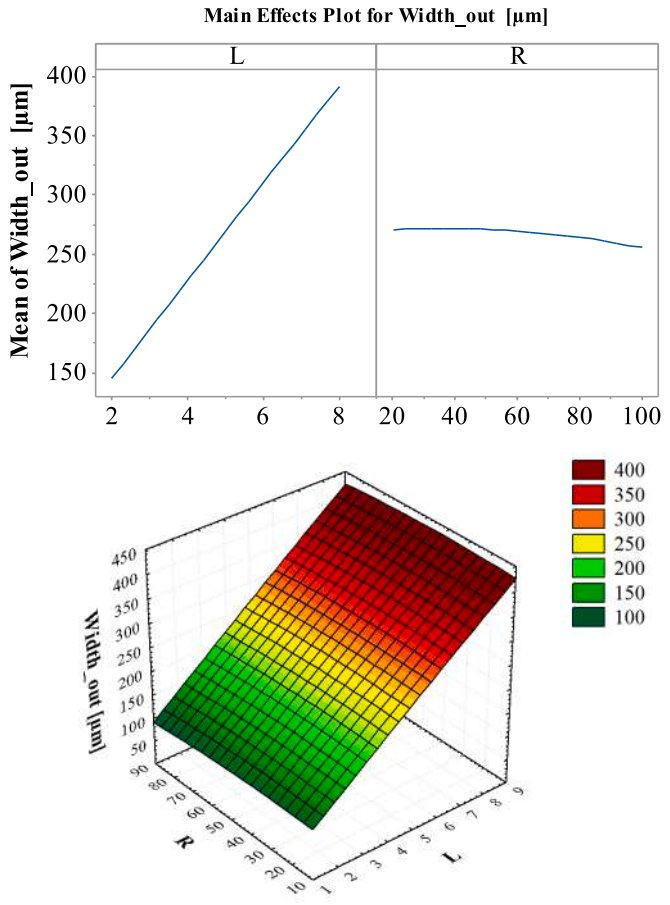

Fig. 9. Main effect plot and response surface for Width_out.

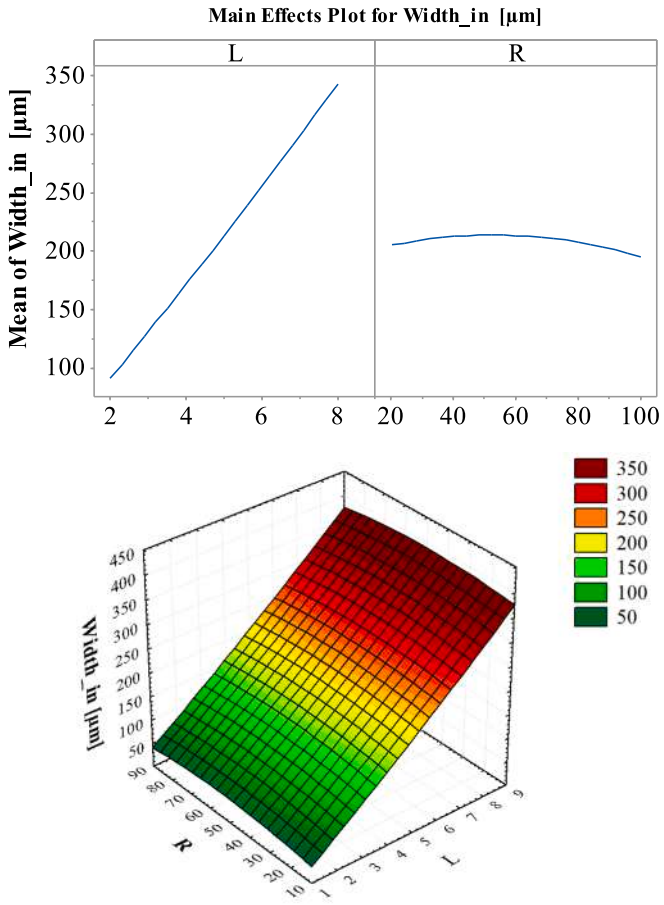

Fig. 10. Main effect plot and response surface for Width_in.

From the grooving tests, two different laser textures were selected for the surface treatments, hereafter named TX1 and TX2. Both treatments adopt parallel grooves placed at 90° to the load direction, the same nominal depth (about 60 µm), a filling factor (FF) of 50% (i.e. the ratio between the grooved and the total surface), and different grove widths (about 140 µm and 400 µm, respectively). All treatments were carried out on a 25x25 mm^2 portion of the titanium sample surface addressed for joining, according to the schematic in Fig. 7.

To discriminate the treatment effect (i.e. the joint resistance), tensile tests were carried out according to the ASTM Standards [33–35], at a displacement ratio of 1.3 mm/min, adopting a Universal testing machine (MTS INSIGHT 5) equipped with a 50 kN load cell. After the tests, the apparent shear strength (Strength), calculated as the ratio between the maximum load and the bonded area, and the energy absorbed up to the failure (FE), calculated as the area under the load/displacement curve, were adopted as response variables. Moreover, digital microscopy (HIROX KH 8700) was utilised to observe and measure the texture geometries and classify the joints' failure mode according to the ASTM D5573-99 Standard [44].

In addition to the two textures, further treatments were considered by adding a laser cleaning phase to the texturing one, either before or after the texturing. The cleaning step involves filling the entire surface of the sample. This process was carried out adopting the 'mark on fly' procedure, which involves moving the laser beam along parallel trajectories spaced in the X and Y direction by a fixed value (Hatch distance or Hd). The laser cleaning process was carried out adopting the following process parameters: pulse energy = 1 mJ, Hd = 50 µm, Ss = 1500 mm/s, f = 30 kHz, with a single repetition (R = 1). These conditions, established through preliminary tests, are primarily aimed at

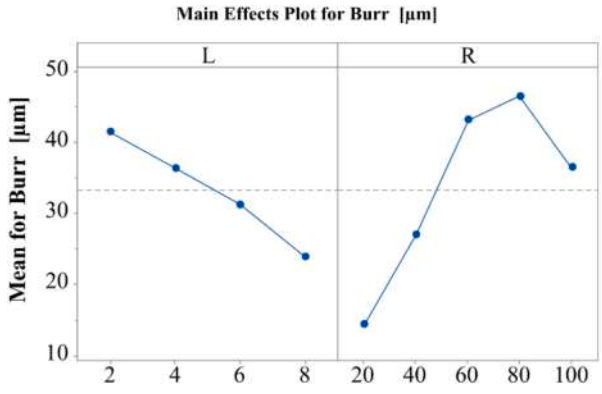

Fig. 11. Main effect plot for Burr.

removing contaminants and oxides present on the as-built materials and the debris (such as dross and droplets) and oxides produced during the texturing process without significantly altering the roughness. Consequently, the treatment provides a new, fresh surface that can enhance adhesion, as observed in [12,23,32]. However, during the process, a micro-texture and an increase in the roughness are also produced. Additional samples were fabricated adopting only the laser cleaning step or mechanical abrasion, first by 240 mesh and then 120 mesh sandpapers (SP samples) polishing. The SP samples were adopted as a reference standard, according to the procedure indicated by the adhesive producer [45]. Table 4 reports the process conditions adopted for the surface treatments of the adherend. Four samples were produced and tested for

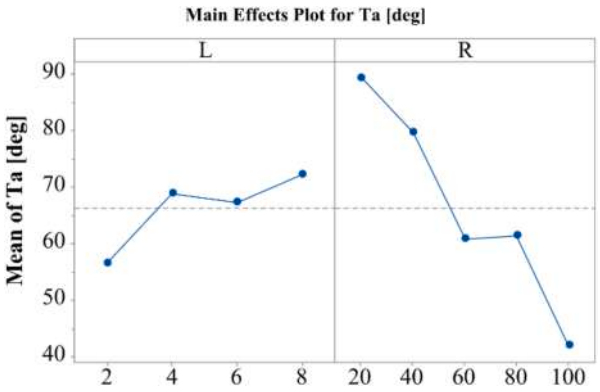

Fig. 12. Main effect plot for Taper Angle.

each set of process conditions, except for the SP treatment, for which three samples were available. One-factor ANOVA and Tukey's method for multiple comparisons were adopted to study the effects of the treatments on the joint strength. Also in this case, the analysis was conducted with a confidence level of 95% ($\alpha = 0.05$), and the ANOVA assumptions were successfully verified through residual analysis. Furthermore, measurement of the roughness (Ra and Sa parameters), contact angle (with 100% glycerol) and chemical composition (by X-ray spectroscopy, through a Scanning Electron Microscope SNE ALPHA, SEC Co. Ltd, equipped with the Xplore compact EDS detector from Oxford Instruments) were carried out on some samples to explain the joint behaviours.

3. Results

3.1. Laser texture and laser cleaning characterisation

3.1.1. RSM model

The Response Surface Model (RSM) is a statistical technique used to

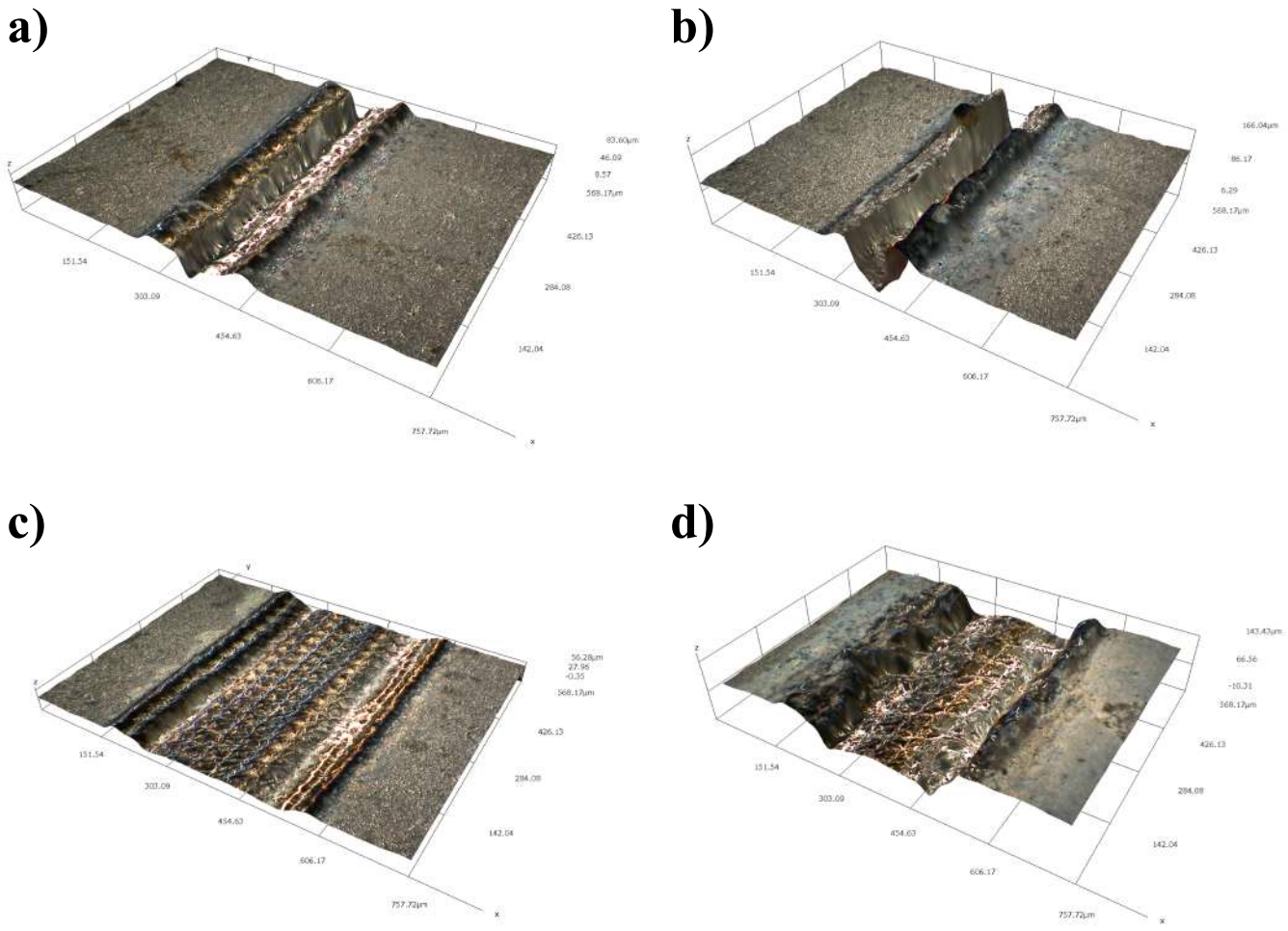

Fig. 13. Images of the grooves at: a) L = 2 and R = 20; b) L = 2 and R = 100; c) L = 8 and R = 20; d) L = 8 and R = 100.

Table 7
Characteristics of adopted texture.

Texture code	L	R	FF%	Depth [µm]	Width_out [µm]	Width_in [µm]	Burr [µm]	Taper Angle [Deg]	HD [µm]
TX1	2	60	50	$67{,}50^{\pm 4.46}$	$141.39^{\pm 2.13}$	$85.94^{\pm 2.13}$	$48.40^{\pm 10.86}$	$47.83^{\pm 12.29}$	300
TX2	8	60	50	$60{,}00^{\pm 2.59}$	$397.73^{\pm 4.39}$	$337.05^{\pm 13.37}$	$35.69^{\pm 9.21}$	$65.78^{\pm 4.47}$	800

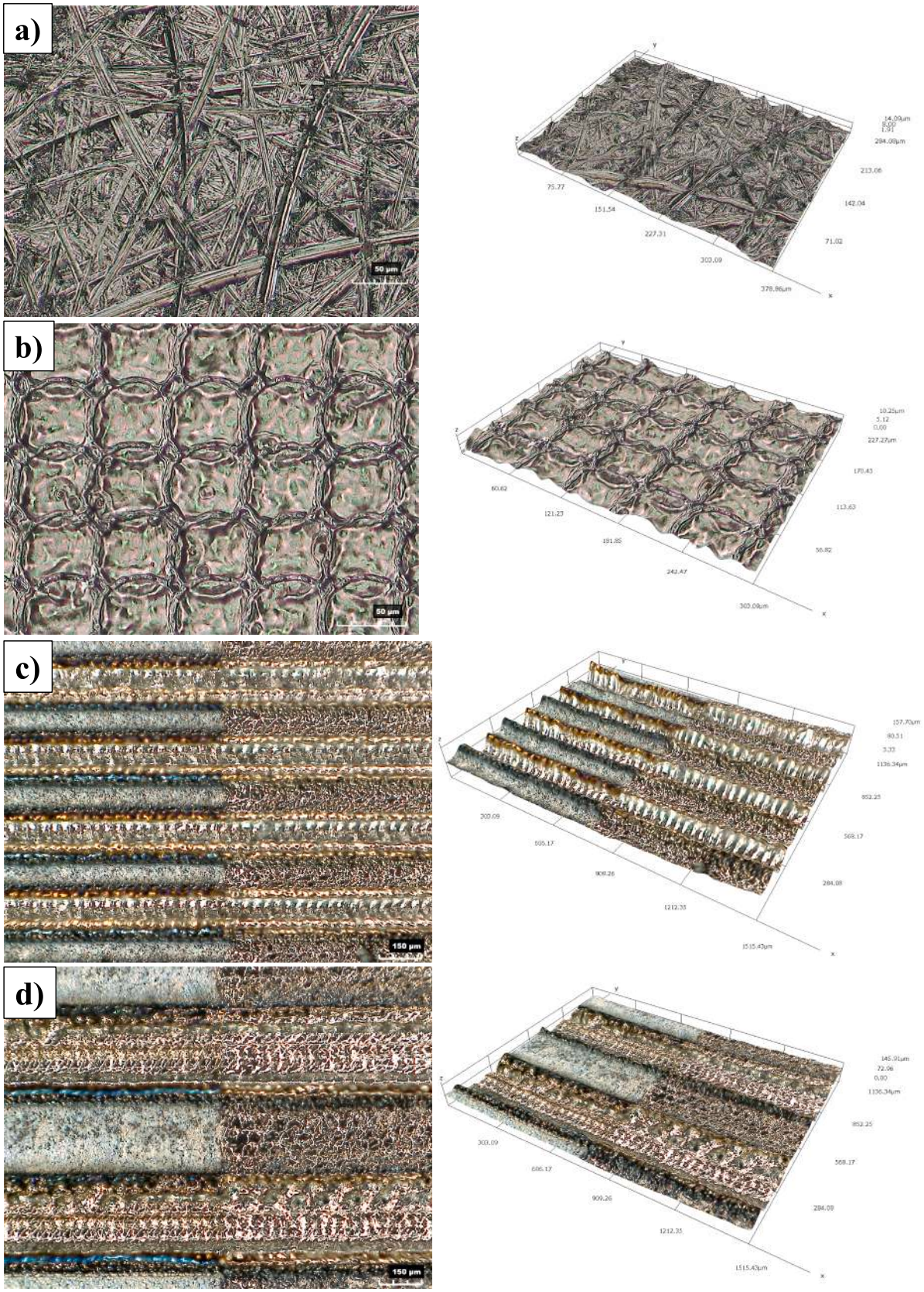

Fig. 14. Images of selected textures. a) SP treatment, b) LC treatment; c) TX1 and TXC1 treatments; d) TX2 and TXC2 treatments.

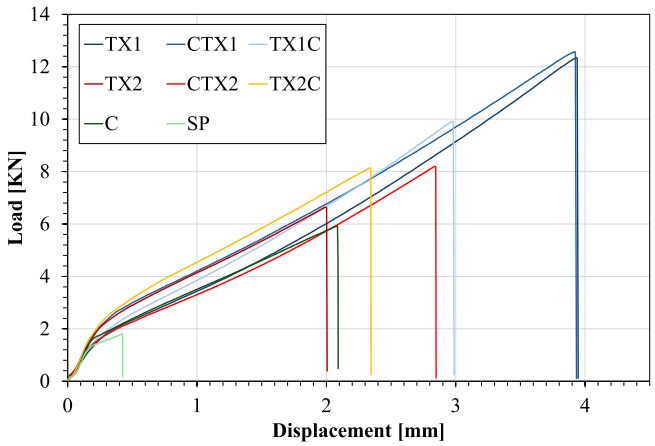

Fig. 15. Load-displacement curves for the different treatments.

Table 8
Observed failure mode.

Failure Mode	Symbol	Description
Adhesive	A	Separation occurs at the matrix-adherent interface
Thin-Layer Cohesive Failure	TLC	Failure is very close to the matrix-substrate interface, characterised by a matrix thin layer on the Ti surface.
Light Fibre-Tear Failure	LFT	Failure occurs exclusively within the FRP matrix, characterised by the appearance of reinforcing fibres and matrix on the Ti adherend surfaces.
Fibre-Tear Failure	FT	Failure is like the LFT one, with a major quantity of fibres on the Ti adherend surfaces.
Cohesive Failure in CFRP adherend	CF	Failure occurs at the CFRP plies' interfaces.

identify the significant control factors (i.e. the process parameters that statistically affect the process) and, simultaneously, to develop a predictive model for estimating their effect on the response variables. The model consists of a set of linear or quadratic equations that allow understanding or mapping a region of a response surface, identifying the control factors' levels that optimise one or more response variables, and selecting the operating conditions to meet specific requirements [42,43]. To obtain a quadratic model, at least three levels for each control factor must be adopted. Fractional factorial designs, such as Central Composite Design or Box-Behnken designs, which require fewer trial numbers, may also be adopted. However, due to the simplicity in sample production and analysis, a full 4 × 5 full factorial design was adopted. The latter has the advantage of delivering a more precise and statistically robust model.

Table 5 shows the results of the ANOVA for the grooves' geometries. From the table, both L and R are significant for all the control factors. However, the significance varies across the control factor, as indicated by the large differences in F-values, spanning one or more orders of magnitude. In detail, the F-value of parameter R is significantly greater for depth and burr. This suggests that R plays a dominant role in affecting these two specific parameters. Conversely, L exhibits an F-value approximately two orders of magnitude greater than that of R when considering both width-in and width-out parameters. This suggests that L exerts a substantially greater influence on the widths compared to R. Furthermore, in the case of burr formation, both R and L exert an influence of comparable magnitude, as their F-values are within the same order. This suggests that both contribute to a similar extent. The term L × L is significant for the Depth, while the term R × R is significant for Width_in and Burr; these terms indicate the presence of a curvature in the surface. In addition, the L × R interaction is statistically

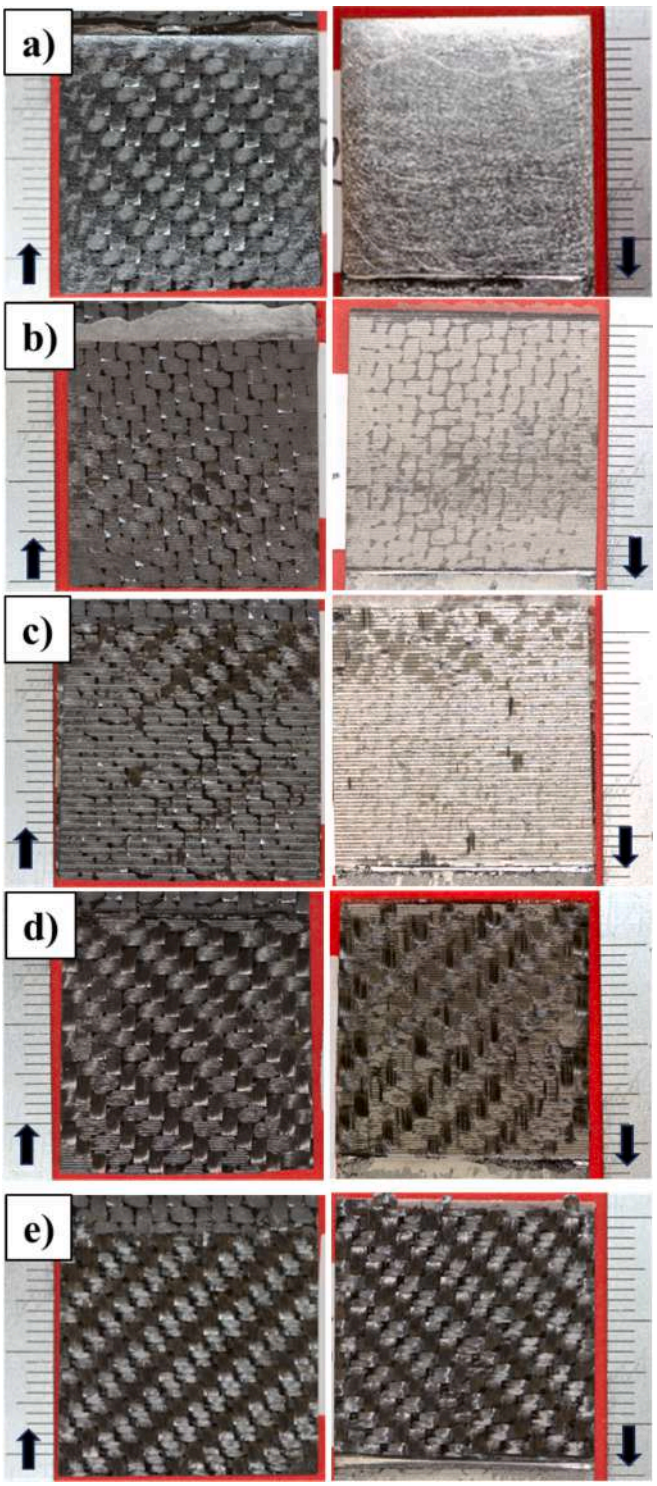

Fig. 16. Examples of failure mode: a) Adhesive failure on a SP sample; b) Thin cohesive failure on a TX1C sample; c) Light Fibre tear failure on a CTX2 sample; d) Fibre tear failure on a CLT1 sample; e) Cohesive failure on a TX1 sample. In the figures, the arrows indicate the direction of the load.

significant for Burr, indicating that the variation in response across the levels of one factor is not consistent across all levels of the other factor. Furthermore, all the significant quadratic terms (R × R and L × L) and the single interaction (L × R) showed a low F-value; consequently, their impact was less dominant than the aforementioned factors of the model (R and L). An exception was represented by Burr, where the term R × R has an equal order of magnitude to L and R, showing a similar impact on

Table 9
Failure mode and failed sample for each surface treatment type.

Treatment	Texture type	Pre-treatment	Post-treatment	Sample n° for failure mode				
				A	TLC	LFT	FT	CF
SP	Sandpaper	No	No	3				
C	Cleaning	No	No		1	3		
TX1	Texture 1	No	No				2	2
CTX1	Texture 1	Cleaning	No		1	1	2	
TX1C	Texture1	No	Cleaning		1	3		
TX2	Texture 2	No	No			1	3	
CTX2	Texture 2	Cleaning	No			3	1	
TX2C	Texture 2	No	Cleaning			1	3	

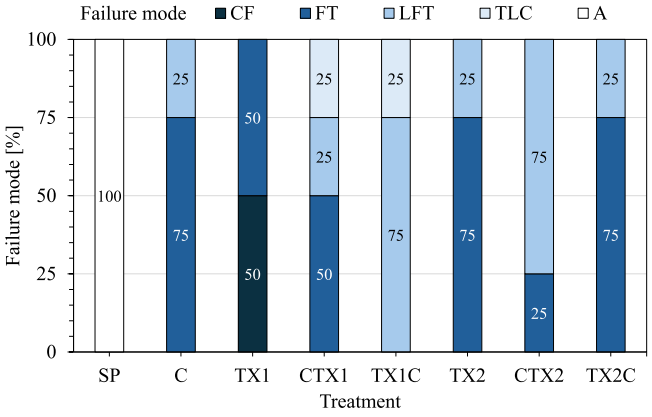

Fig. 17. Failure mode percentage for the different surface treatments. A = Adhesive; TLC = Thin-Layer Cohesive Failure; LFT = Light Fibre-Tear Failure; FT = Fibre-Tear Failure; CF=Cohesive Failure in CFRP adherend.

the response. However, the quadratic term only indicates the presence of a curvature. Table 5 also provides the error estimators: R-sq, R-sq(adj), Rsq[adj], and Rsq[pred]. R-sq describes the amount of the response variable variation explained by the control factors, the R-sq(adj) is a modified R-sq that has been adjusted for the number of terms (replication and levels) in the statistical model, while the R-sq(pred) shows how good the correlation between the experimental and model values: a high R-sq(pred) indicates a good correlation. From the table, the Depth, Width_out, and Width_in present an adequate level of R-sq, Rsq[adj], and Rsq[pred]. Conversely, the burr and taper angle show low Rsq [pred] values, about 76% and 54%, respectively. This means that the model is not accurate enough to estimate/model the Burr and the Taper angle. Consequently, the latter were discharged from the RSM analysis. The limited accuracy of the RSM models is primarily due to the difficulty in measuring both Ta and the burr. Moreover, the burr exhibits significant variability along the groove profile. As a result, these parameters are subject to considerable data scattering, which the model reflects as low predictive accuracy, indicated by a low Rsq[pred] value. However, given that the statistical significance of the control factors is assessed using the p-value, the influence of the process parameters on Burr and Ta was studied through the analysis of the main effect plot, carried out directly on the experimental data. In addition, since the interaction L × R for the burr shows an F-value one order less than the main factor, the interaction plot was discarded from the analysis.

As previously mentioned, one of the advantages of RSM is the ability to provide a second-order regression model. These equations relate the control factors (L and R) and their products (L^2, R^2, L × R) to the response variables (Depth, W_out, W_in) through six constants (K1, K2, …, K6) [42,43]. The basic equation is the following:

$$Source = K1 + K2 \cdot L + K3 \cdot R + K4 \cdot L \times L + K5 \cdot R \times R + K6 \cdot L \times R \quad (1)$$

where the term "Source" indicates the response variable. Table 6 summarises the equations for the three response variables. These equations

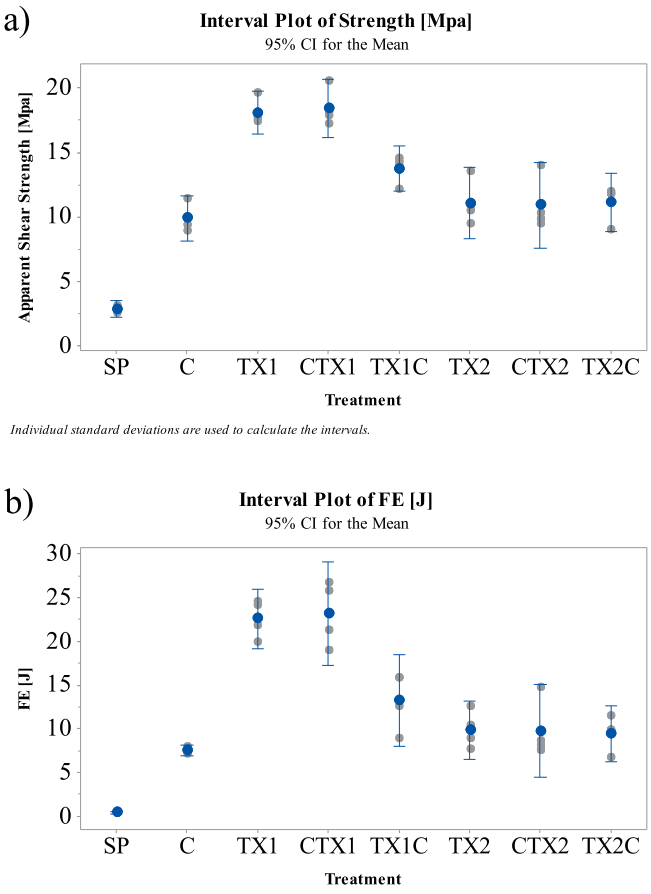

Fig. 18. Interval plot for: a) Strength; b) Failure Energy. AB samples are not reported.

Table 10
ANOVA table for Strength and Failure Energy.

Response variable	Source	DF	Adj SS	Adj MS	F-Value	p-Value
Strength	Treatment	7	610.09	87.156	43.77	**0.000**
	Error	23	45.79	1.991		
	Total	30	655.89			
	R-sq [%]		93.02			
	R-sq(adj) [%]		90.89			
Failure Energy	Treatment	7	1504.9	214.989	33.84	**0.000**
	Error	23	146.1	6.353		
	Total	30	1651.0			
	R-sq [%]		91.15			
	R-sq(adj) [%]		88.46			

a)

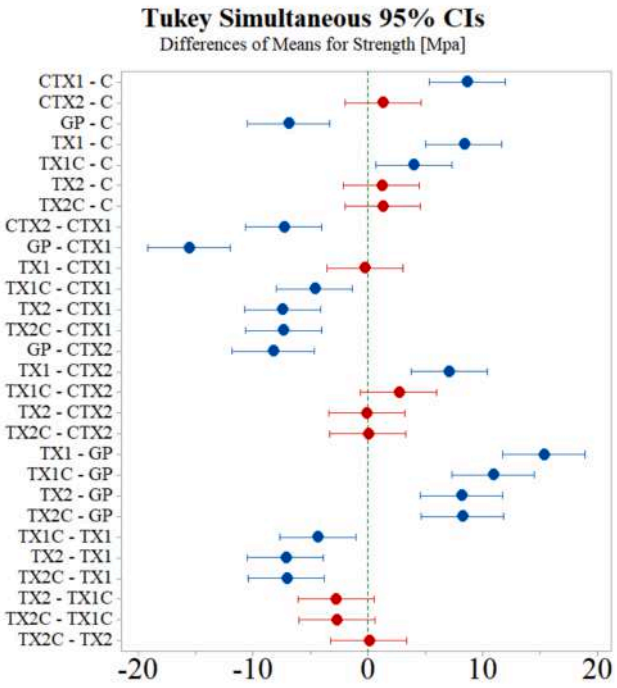

b)

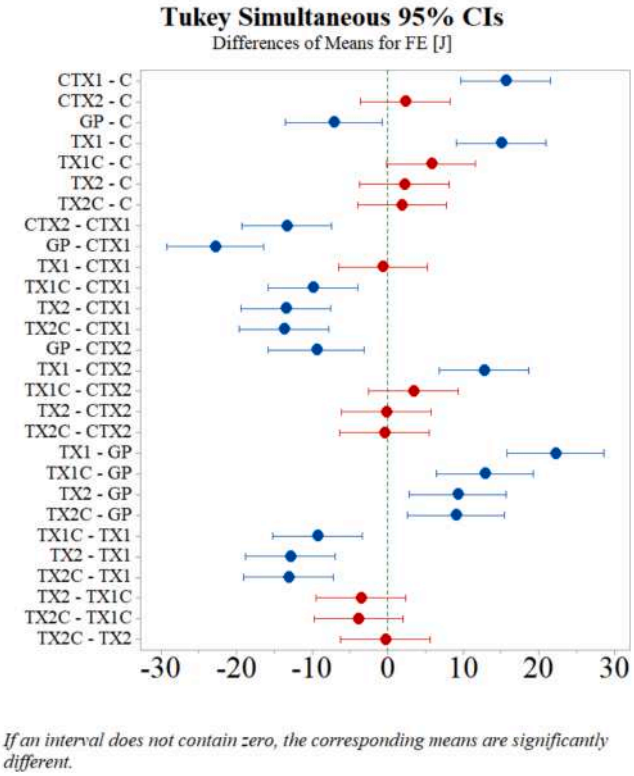

Fig. 19. Results of Tukey comparison for the laser-treated samples: a) Strength; b) Failure Energy. SP samples are not shown in the diagrams.

Table 11
Tukey comparison, computed value and grouping for the apparent shear stress.

Treatment	N	Mean [Mpa]	St.Dev [Mpa]	95% CI [Mpa]	Grouping		
CTX1	4	18.453	1.453	**17.00—19.91**	A		
TX1	4	18.116	1.028	16.66—19.57	A		
TX1C	4	13.757	1.116	12.30—15.22		B	
TX2C	4	11.112	1.421	9.65—12.57		B	C
CTX2	4	11.076	1.759	9.62—12.53		B	C
TX2	4	10.91	2.11	9.46—12.37		B	C
C	4	9.891	1.094	8.43—11.35			C
SP	3	2.816	0.269	1.13—4.50			D

Table 12
Tukey comparison, computed value and grouping for the failure energy.

Treatment	N	Mean [J]	St.Dev [J]	95% CI [J]	Grouping		
CTX1	4	23.17	3.70	20.56—25.78	A		
TX1	4	22.57	2.13	19.96—25.17	A		
TX1C	4	13.24	3.31	10.63—15.85		B	
CTX2	4	9.82	2.09	7.21—12.42		B	
TX2	4	9.68	3.34	7.07—12.28		B	
TX2C	4	9.39	1.98	6.79—11.99		B	
C	4	7.48	0.37	4.87—10.09		B	
SP	3	0.351	0.06	−2.66—3.36			C

were adopted to produce the main effect plots and the response surface plots discussed in the next paragraph.

3.1.2. *Effect of process parameters on groove geometries*

In Figs. 8-10, the main effect plot and the response surfaces derived from RSM analysis are reported, for Depth, Width_out, and Width_in, respectively; while in Fig. 11-Fig. 12, the main effect plots derived from the analysis of the experimental data for the Burr and Taper angle are reported. To explain the relationship between the process parameters and the groove geometry, it is necessary to consider the laser-material interaction mode and the removal mechanisms. The adopted laser releases pulses up to 20 kW (a pulse energy of 1 mJ @ 50 ns), corresponding to a power density of 10^8 W/cm^2. According to [46,47], at this power density, the energy absorbed by the material is high enough to generate material melting and vaporisation, as well as the formation of high-pressure plasma. Then, due to the high plasma pressure (the so-called recoil pressure [48]), part of the melted materials pulls out of the groove towards the surrounding area, forming the burr. Therefore, the typical Gaussian-like marks, characterised by rim (i.e. the burr), are generated. Obviously, by performing more laser scanning, one close to the other, the groove tends to widen, but the removal mechanisms remain the same. Then, since in the adopted condition, each repetition (R) can machine a certain quantity of material which must be added to the previous one, the Depth increases with the R increase (Fig. 8). Conversely the effect of L be explained considering that for large groove (high L value) only a part of the molten material is blow out by the vapours pressure on the grove side, the remainder tends to settle on the internal surface of the groove (as also confirmed by the W profile of Fig. 6b) resulting in a depth reduction. Since this quantity depends on how far the machined area is from the edge of the groove, i.e. on the number of lines (L) adopted in the groove production, this effect increases with the increase of L, as visible in Fig. 8.

Fig. 9 and Fig. 10 show the effect of L and R on the Width_out and Width_in. As expected, the width increases linearly with the number of lines (L), since the greater the number of lines, the wider the machined area (i.e. the groove width). Conversely, the increase in the number of repetitions results in a moderate decrease in the widths, especially for high R values. Moreover, the effect is more visible for Width_out than for Width_in. The latter happens since the widths are measured between the side parts, where, due to the recoil pressure, the molten material is

Table 13
Roughness parameters (Ra) and Contact angle values (θ) for the AB, SP, and C samples.

Treatment	Ra [μm]	St.dev. [μm]	95% CI	θ [deg]	St.dev. [deg]	95% CI
As-built (AB)	0.47	0.044	0.446–0.499	96.58	4.85	94.03–99.13
Sandpaper (SP)	0.26	0.020	0.236–0.289	32.35	1.932	29.60–35.10
Laser cleaning (C)	0.56	0.039	0.536–0.589	6.083	0.624	3.33–8.84

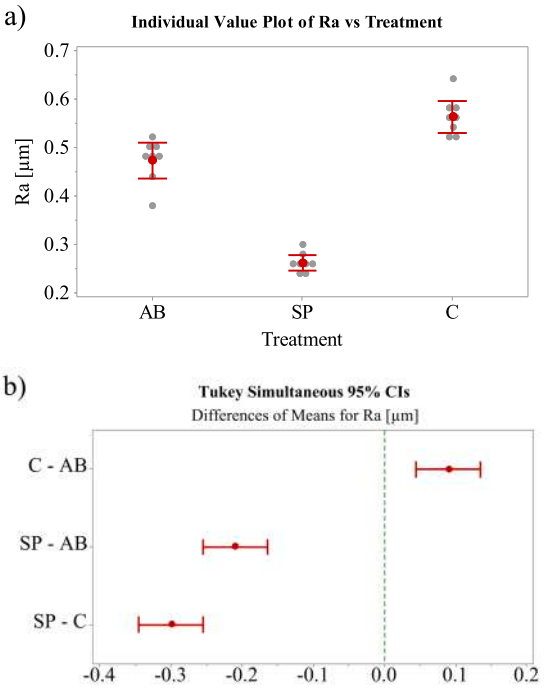

Fig. 20. Ra parameter: a) Individual value plot; b) Tukey comparison plot.

deposited. As previously explained, increasing the number of repetitions increases the groove depth; consequently, the melted material pushed by the recoil pressure faces difficulty in pulling out of the groove and tends to deposit inside and on the edges of the same. This effect involves a reduction in the groove's width, which is more sensitive at high L values, i.e. the wider the groove is.

From Fig. 11, the height of the burr tends to reduce as L increases (i.e. an increase in the width of the groove), while increasing R until it reaches a maximum at R = 80, and then stabilises. The reduction observed as L increases is primarily due to the corresponding increase in groove width, which causes part of the molten material to settle towards the groove centre, resulting in the formation of a lower and asymmetric burr. (i.e. higher in the area where the last scan is present, as clearly visible in Fig. 6b). The effect of R is explained by considering that during the first passes (for R = 20–80) of the laser, the depth of the groove is low enough to allow the melt to pull out from the grooves easily and to settle on the edge forming the Burr. Further increase (R > 80) in depth leads to greater difficulty in the melt's escape; consequently, the growth of the burr tends to slow down, and its height tends to be stabilised. The taper angle essentially depends on how deep and wide the groove is, considering that for L = 2, the groove has an approximately Gaussian shape, while for L > 2 the groove shows a trapezoidal shape (as visible in Fig. 6). Therefore, since an increase in the number of repetitions leads to a linear increase in depth a linear reduction in the taper angle results (Fig. 12). Conversely, the L increase leads to an increase of the width, and, therefore, to an increase of the Taper angle.

However, since the groove shape changes from triangular to trapezoidal, the rate of increment decreases with increasing width, resulting in the trend shown in Fig. 12. This also accounts for the differences between the F-value parameter found in Table 5.

Fig. 13 shows some images of grooves obtained at L = 2 and L = 8, at R = 20 and R = 100. It's worth noting that when R = 100 (Fig. 13b and Fig. 13c), the surface of the component is characterised by the presence of oxides. These oxides are due to the greater quantity of energy released for R = 100, which results in higher temperatures of the substrate, and the production of sprays and vapours of the metal during laser-material interactions, which tend to settle on surrounding surfaces.

3.1.3. *Selected treatments*

The textures were selected based on the previous experience [45,49], main bibliography [26] and preliminary tests, considering that:

i) shallow or deep grooves do not necessarily lead to strength improvements. The former does not permit effective failure, as they neither significantly increase the area involved in fracture propagation nor ensure complete groove filling [27,28]. Concerning the latter, exceeding a certain depth, the failure occurs in the resin's section, which does not change with the depth, then a further depth increase does not lead to an improvement in resistance, but only to an increase in process time;
ii) the presence of a certain burr height increases the effect of the mechanical anchoring [45,49,50] but, at the same time, increases the local stress and the peeling components [51,52];
iii) the filling factor, i.e. the ratio between the machined area and the total area available for joining, determines, of course, the treated area percentage, and, together with the groove width, the number of grooves and burrs (the hooks) useful to produce the mechanical anchoring;
iv) the groove width controls the number of grooves/burrs per unit length, and the hooks' working section. Then, it will be preferable to produce narrow grooves. However, it should be noted that a too narrow groove may result in incomplete resin filling [27,28], while a large groove may facilitate the penetration of the carbon tow in the grooves and its contribution to the strength.

Then, the depth and the filling factor were fixed at 60 μm and 50%, respectively, and the groove's width was selected at two levels: 140 and 400 μm. Furthermore, as texture geometry, parallel lines orthogonal to the load direction were adopted, according to the results obtained in [29]. It is worth noting that the first texture type (TX1 texture) allows a great number of grooves and burr. Then it maximises the number of anchor points; the second one (TX2 texture) was used to verify whether an increase in the groove width allows for carbon tow penetration and, subsequently, the possibility of having a greater contribution from the reinforcement (i.e. carbon fibres). Table 7 summarises the characteristics of the two textures.

Moreover, since the strength of a joint depends not only on the mechanical anchoring effect but also on how the resin adheres to the surface, as aforementioned, the adoption of laser cleaning treatment has been added to the two textures. The latter has the purpose of enhancing adhesion on untreated surface regions and, when applied after the texturing, to remove oxide and debris generated during the texturing operation from the surface. Then, the laser cleaning was adopted as a single treatment (C) or in combination with laser texturing in both configurations: before and after the texturing phase (see also Table 4). In Fig. 12, the magnifications of some treatments are reported. In the

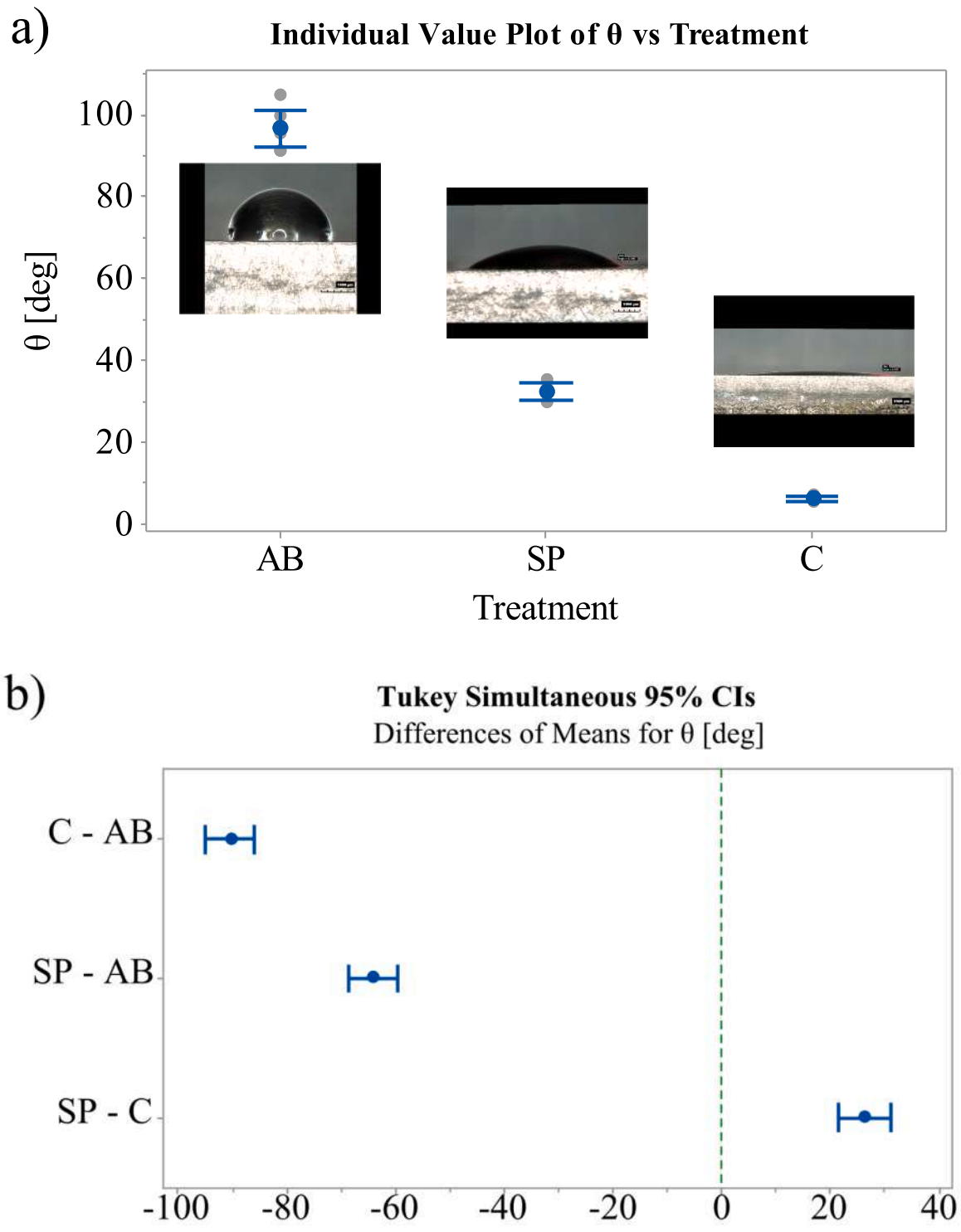

Fig. 21. Contact angle (θ) parameter: a) Individual value plot; b) Tukey comparison plot.

figures, to highlight the effect of laser cleaning on the textured surface, the right-hand side of the TX1 and TX2 samples (Fig. 14c and Fig. 14d) shows the impact of the laser cleaning post-treatment application. From Fig. 14, looking at the left side, laser texturing involves the formation of a white and blue deposit between the grooves, which consists of molten material expelled during laser machining, recondensed vapours, and oxides. Looking at the right side (where the laser cleaning post-processing was performed), the deposits are absent, and the material appears light/bright grey. A similar effect occurs when the surface is subjected solely to the laser cleaning treatment, as shown in Fig. 14b.

Table 14
Chemical composition measured through EDX analysis on the sample surfaces (only elements with a weight percentage > 0.5%).

Element wt%	Treatment								
	AB	SP	C	TX1	CTX1	TX1C	TX2	CTX2	TX2C
Ti	85.15	86.92	77.66	68.22	62.72	65.05	63.87	63.31	70.12
O	4.80	3.80	13.22	24.72	30.38	28.13	29.76	30.50	22.98
Al	6.55	5.78	5.79	3.97	3.77	4.01	3.57	3.48	3.92
V	3.50	3.50	3.33	3.09	3.13	2.81	2.80	2.71	2.97

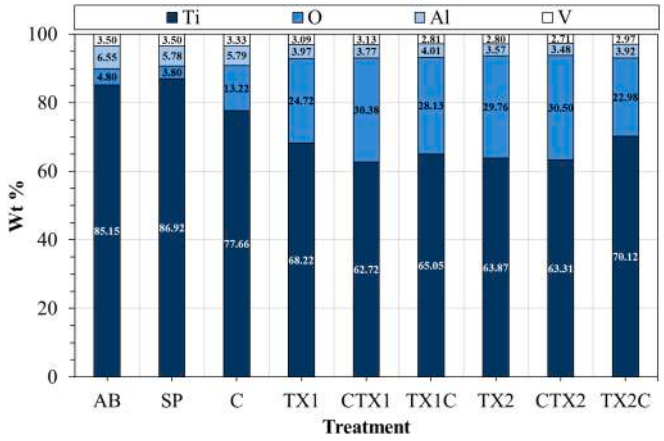

Fig. 22. Average chemical composition (only elements with a weight percentage > 0.5%).

3.2. Results of tensile test

3.2.1. Stress-displacement diagrams and failure mode

Representative load–displacement curves for the various surface treatments are presented in Fig. 15.

Regarding the slope of the load–displacement curves, all tested samples exhibited similar behaviour, indicating comparable stiffness across the surface treatments. However, the samples treated through Texture 1 (including the ones with the additional laser cleaning phase) demonstrated the best performance, whereas the sandpaper treatment resulted in the lowest bonding strength.

After the testing, the failure modes were classified according to the ASTM D5573-99 Standard [44]. The observed failure modes are reported in Table 8, while Fig. 16 shows some examples of failed surfaces. It is worth noting that only the SP treatment showed adhesive failure. Conversely, all the laser treatments have shown cohesive failure, albeit with different modalities of reinforcement involvement.

Table 9 collects the failure mode occurrences for the different treatments. The same data are presented as failure mode percentage in Fig. 17. From the figure, sandpaper samples exhibited adhesive failure across all tested specimens, indicating poor adhesion between the alloy and the adhesive. In contrast, laser treatments effectively change the failure mode, enhancing the contribution of the CFRP fibres to the bonding performance. Laser cleaning alone facilitated a transition from adhesive failure to thin-layer cohesive failure or light fibre-tear failure. Furthermore, all textured samples predominantly exhibited fibre tear failure (at least three out of four samples), indicating enhanced adhesion and joint performance. It is worth noting that the TX1 treatment resulted in cohesive failure within the CFRP (interlaminar failure) in two out of four specimens, indicating a superior bonding strength and adhesive integrity.

3.2.2. Apparent shear strength and failure energy

In Fig. 18 the interval plot of the apparent shear strength (Fig. 18a) and the failure energy (Fig. 18b) are reported; the treatments that showed the best bonding performance in terms of apparent shear strength were the ones characterised by the narrowest groove, in particular the TX1 and the CTX1 samples, that results in an Apparent

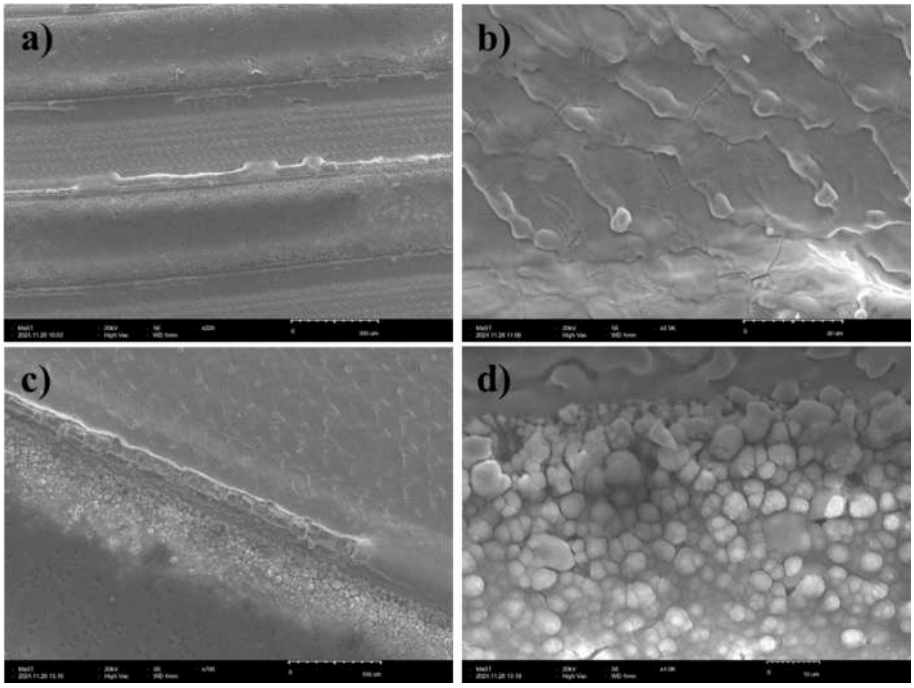

Fig. 23. SEM images of TX2 sample: a) Overall surface at 220X; b) Inside the groove; c) close to the burr; d) Burr bottom at the external groove side.

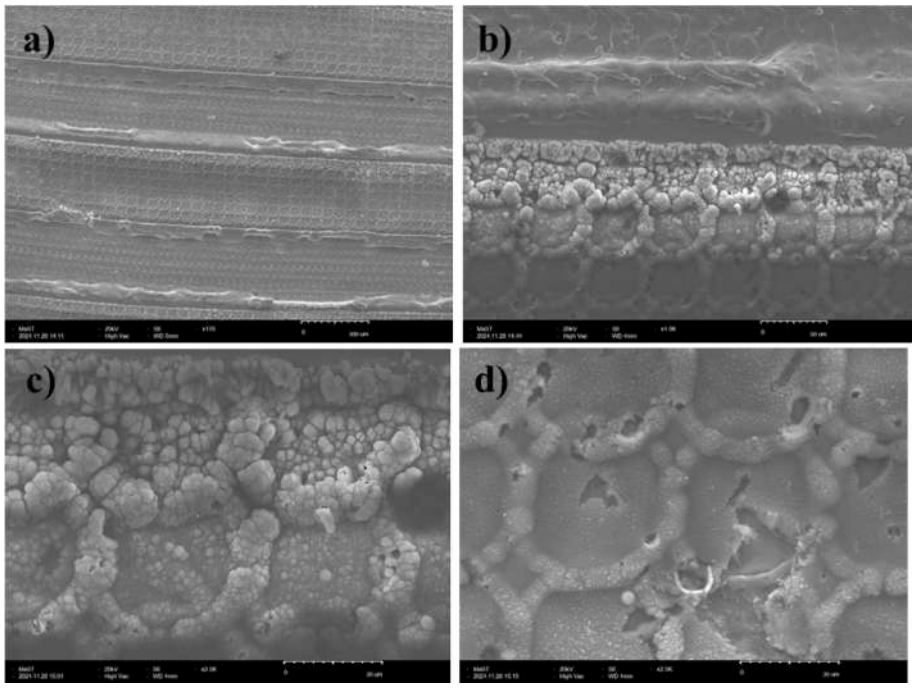

Fig. 24. SEM images of CTX2 sample: a) Overall surface at 170X; b) Straddling the burr; c) Straddling the burr; d) Between two grooves.

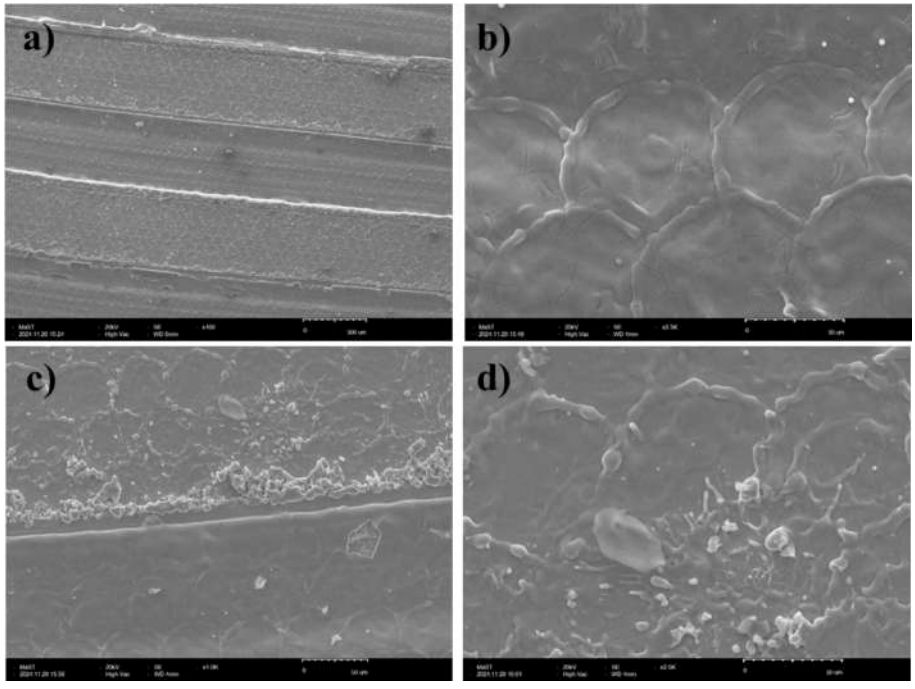

Fig. 25. SEM images of TX2C sample: a) Overall surface at 160X; b) Inside the groove; c) Straddling the burr; d) Between two grooves.

Shear Strength of about 18 MPa. Conversely, the sandpaper treatment showed the lowest apparent shear strength (3 MPa). The other laser treatments show average Strength in the range 11–13 MPa. Regarding the Failure Energy, the behaviour is comparable: samples TX1 and CTX1 exhibit the highest value (approximately 23 J), theSP treatment shows the lowest (around 0.3 J), while the remaining treatments fall within the range 7–13 J.

The one-way ANOVA and Tukey's multiple comparisons were adopted to analyse the Apparent Shear Strength (Strength) and Failure Energy (FE). The ANOVA tests for significant differences between the means of the response variables by partitioning their total variation into different sources (error, experimental group membership, etc.), while the Tukey's multiple comparisons method was adopted to reduce the Family Errors. The family error is the maximum probability that a procedure involving more than one comparison will incorrectly conclude that at least one of the observed differences is significantly different from the null hypothesis. Tukey's method creates confidence intervals for all pairwise differences between factor level means while controlling the family error rate to a specified level. It adjusts the confidence level for each individual interval so that the resulting

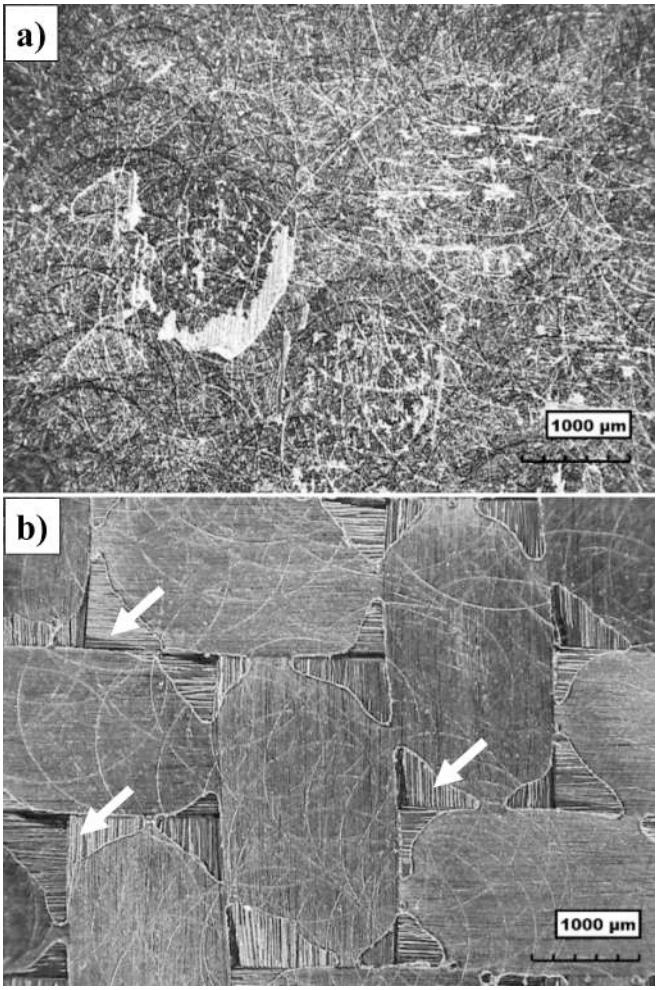

Fig. 26. Magnified view of the failure surface for an SP sample: a) Ti side; b) CFRP side. In the figure, the arrows indicate a lack of resin.

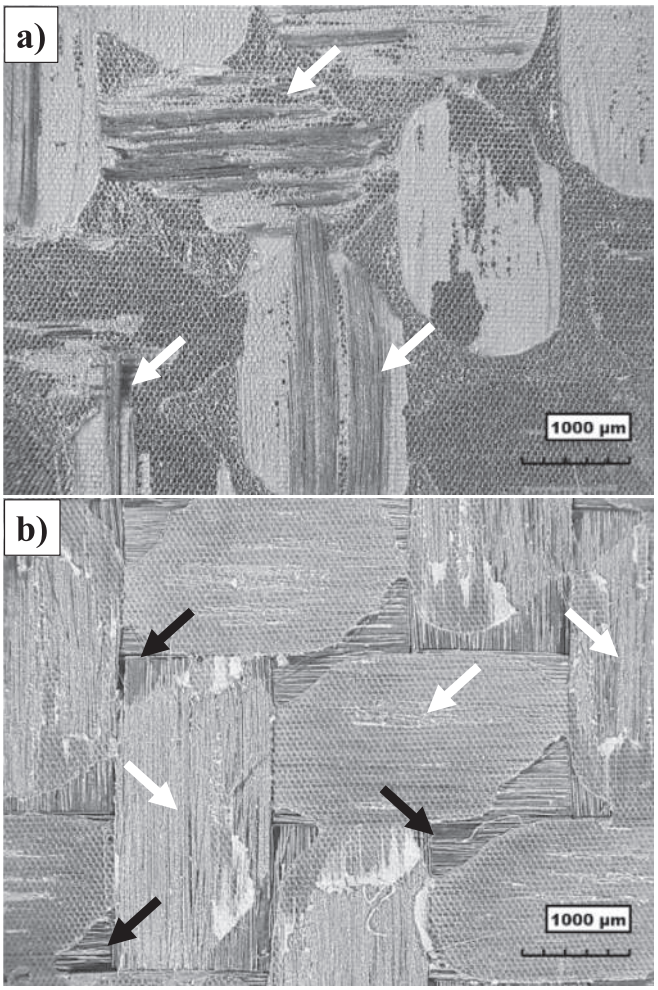

Fig. 27. Magnified view of the failure surface for a C sample: a) Ti side; b) CFRP side. In the figure, white and black arrows indicate fibre failure and a lack of resin, respectively.

simultaneous confidence level matches the specified value. Moreover, it allows categorising the different treatments into distinct groups (grouping). Belonging to a group indicates the absence of statistical differences between the treatments. The ANOVA results for Strength and Failure Energy are summarised in Table 10. From the table, the treatment is significant for both response variables (Strength and Failure Energy), with high R-sq[%] and R-sq(adj)[%] values. However, not all treatments are different from each other, as can be seen from the analysis in Fig. 19, where the results of the Tukey comparison for strength and failure energy are reported. In the diagrams, the treatments are compared individually. If an interval does not encompass the zero value, the corresponding means are significantly different (i.e. significantly distinct). It is worth noting that since the SP treatment differs from all others, it has been omitted to improve the clarity of Fig. 19. The results of Tukey's comparison are also reported in Table 11 and Table 12 for the Strength and the Failure Energy, respectively.

From Table 11, the strength are categorised into four groups: (A) comprising the highest values (CTX1 and TX1); (B) including the treatments TX1C, TX2C, CTX2 and TX2; (C) partially overlapping with group (B), excluding TX1C and adding treatment C; and, finally, D) consisting solely of the SP treatment (the one with the lowest resistance). Table 12 shows the Tukey's comparisons for the Failure Energy (FE), with results grouped as follows: (A) comprising CTX1 and TX1 (approximately 23 J); (B) including the remaining treatments (in the range of 7–13 J), except for the SP, which is the sole member of group (C) whit a very low FE (below 3.36 J).

Results indicate that, irrespective of the texture type and the presence of laser cleaning treatment (whether applied before or after texturing), laser treatments significantly enhance joint strength. The most effective treatments are CTX1 and TX1, which, being grouped within the same category for both strength and FE, are statistically equivalent. Conversely, SP represents the least effective treatment, yielding both low strength and failure energy.

It's worth noting that the Laser Cleaning treatment alone achieved a strength of approximately 10 MPa and a Failure Energy of 7.5 J, which are three and twenty times higher than those obtained with the sandpaper treatment, respectively. Considering that laser cleaning requires significantly less processing time than texturing, these results are particularly noteworthy.

4. Discussion

Different mechanisms are involved in the adhesion process, comprising chemical, physical and mechanical ones. When two components are bonded, the adhesive initially wets the bonding surfaces thoroughly, then fills the gap between them before curing to form a joint. The final strength is, therefore, governed by multiple phenomena: in the first stage, the adhesive must spread uniformly across the component, filling any surface cavities. During the cure, it must establish chemical bonds with the surface, the resistance of which depends on the chemical affinity between the adhesive and the substrate, as well as

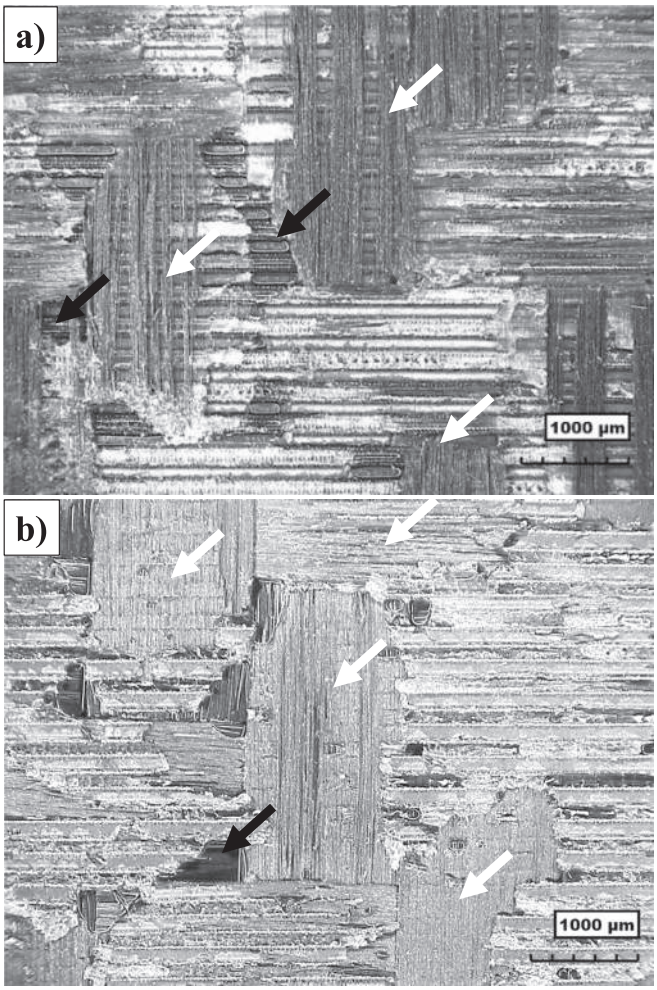

Fig. 28. Magnified view of the failure surface for a TX1 sample: a) Ti side; b) CFRP side. In the figure, white and black arrows indicate fibre failure and a lack of resin, respectively.

the effective area (i.e. the roughness). Additionally, an appropriately rough surface can promote mechanical interlocking [3], which may significantly contribute to overall joint strength. To understand the effects of the different treatments on the adhesion mechanisms, additional tests were conducted on selected samples. In detail, the roughness parameter Ra (according to ISO 21920–3:2021 [53]) was measured for the as-built (AB), Sandpaper (SP) and laser-cleaned (C) samples, through a roughness meter (Taylor Hobson, Surftronic 3^{+}); no less than two measures on three different samples were acquired. Additionally, wettability tests were conducted on the same samples using the contact angle measurement method (ASTM D7334–08/2022 [54]). The apparent contact angle (θ) was measured through the 3D Digital Microscopy Hirox HK8700, according to the procedure reported in [55]. During the test, a 10 µL drop of glycerol (100%) was adopted as a reagent, as its chemical polarity is more comparable to that of epoxy resins than water [56]. No less than six measurements were taken 60 s after drop application. Moreover, chemical analyses were performed on several samples at various points. The measurements were carried out using a scanning electron microscope (SNE ALPHA, SEC Co. Ltd) equipped with an energy-dispersive X-ray spectroscopy (EDS) sensor (Oxford Instruments model Xplore Compact EDS detector).

Table 13 reports the roughness and the contact angles measured on the as-built (AB), SP and C samples, respectively. Fig. 20 and Fig. 21 show the individual value plot and Tukey comparison plot for Ra and the apparent contact angle, respectively. It is worth noting that the one-way ANOVA indicates that the treatment is significant for both response variables (Ra and θ), i.e. the *p*-values are less than 0.000. Furthermore, Tukey comparison confirms that the three treatments differ significantly from each other. Regarding the chemical analyses, Table 14 and Fig. 22 show the average composition of the surface subject to the different treatments, in terms of Titanium (Ti), Aluminium (Al), Vanadium (V), and Oxygen (O) weight percentage. From the analysis, Al and V exhibit small variations in terms of weight percentage. Conversely, the oxygen percentage varies from a minimum of 4–5% for the SP and AB samples, respectively, to approximately 13% for the CL sample, and up to about 30% for the textured ones. Additionally, the samples subjected to the laser cleaning post-treatment (TX1C and TX2C) exhibit lower oxygen levels compared to both those without post-treatment (TX1 and TX2) and those previously treated with laser cleaning (CTX1 and CTX2).

The oxygen concentration on the cleaned (C) sample (13%) indicates the formation of TiO. Regarding the samples subjected to laser texturing, the high Oxygen percentage (>24%) and the observation of Fig. 14 c-d, (see Chapter 3.1.3), suggest the formation of TiO_2 under form of both Anastase and Rutile, that, according to [57], are due the partial conversion of TiO, produced during the first repetitions, in TiO_2 (Anastase) at 450°C, and then in Rutile at 600- 700°C, during the subsequent repetitions. The Rutile presence is also confirmed by the white/blue colours observed on the sample surface (see Fig. 14 c-d) [58–60]. It is worth noting that, for the CTX1 and CTX2 samples, the oxygen content in the area surrounding the burr can reach 36–40%. Nevertheless, the results are consistent with [26,61], which confirms the formation of Ti-oxide during laser treatment. These oxides increase the surface energy of titanium, thereby improving wettability and chemical bonding, as evidenced by the contact angle measurements on the C samples.

A further difference between the textured samples is the structure observable at high magnification: in the only textured samples (TX1 and TX2) the oxides are organised in the form of small crystals, mainly concentrated in the areas adjacent to the burr (Fig. 23 c-d); in the samples where the laser cleaning was previously applied (CTX1 and CTX2), these structures are also present, and are visible like a thin icing,

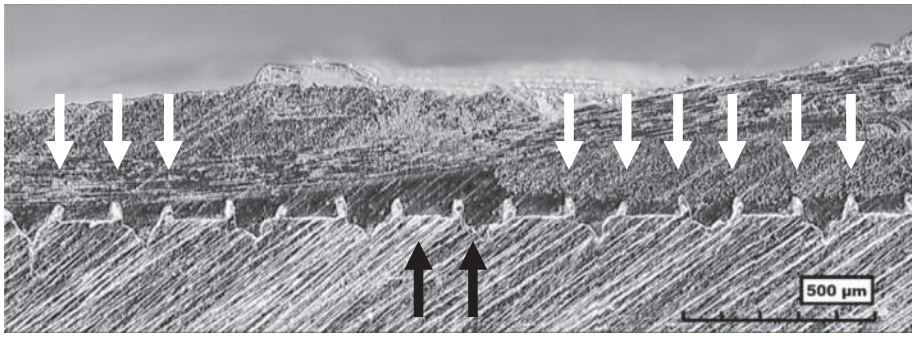

Fig. 29. Cross-section of a TX1 sample failed by "Cohesive Failure in CFRP adherend" mode. In the figure, white arrows indicate mechanical interlocking between the texture and the fibres; black arrows indicate the presence of a matrix cavity in correspondence with the warp and the weft intersections.

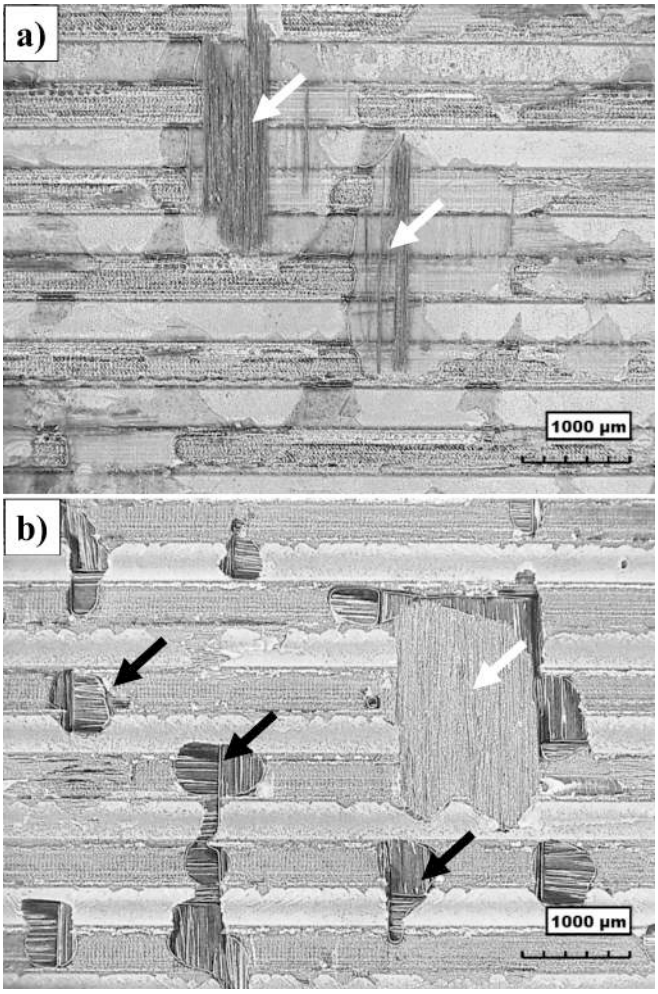

Fig. 30. Magnified view of the failure surface for a TX2 sample: a) Ti side; b) CFRP side. In the figure, white and black arrows indicate fibre failure and a lack of resin, respectively.

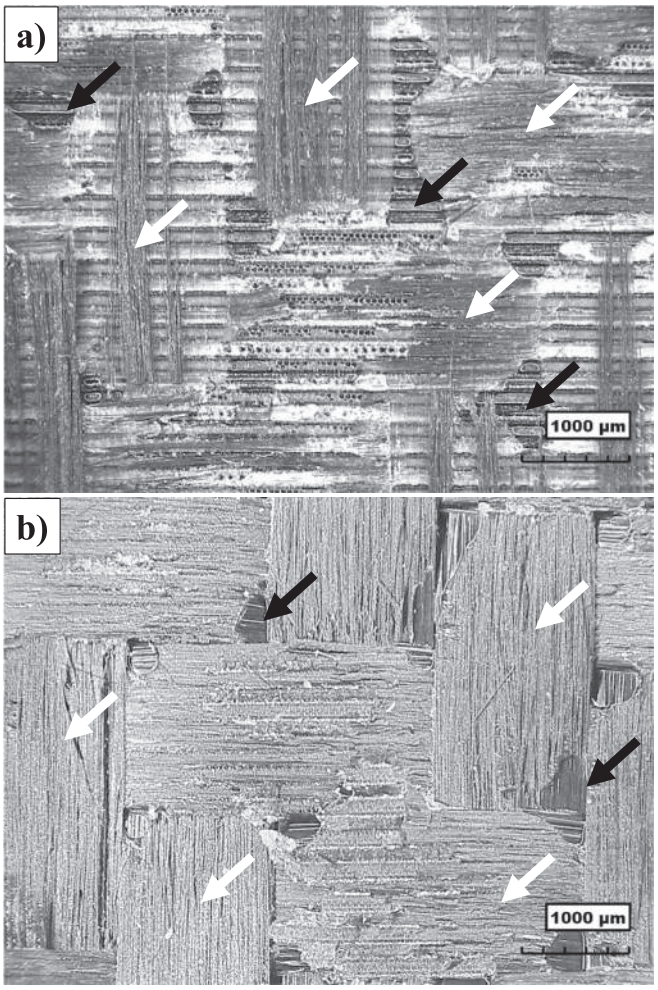

Fig. 31. Magnified view of the failure surfaces of a CTX1 sample: a) Ti side; b) CFRP side. In the figure, white and black arrows indicate fibre failure and a lack of resin, respectively.

in the area between two adjacent grooves (Fig. 24d), as shown by Figs. 11 and 12. Conversely, for the samples cleaned after texturing (TX1C and TX2C), these oxide structures are absent or reduced (Fig. 25). It can therefore be stated that laser cleaning performed after texturing removes part of the oxides (TiO_2) and debris generated during the laser machining process.

Despite the reduction in contact angle obtained with the sandpaper treatment (32° against 96° for the AB one), the surface energy remains insufficient to promote complete matrix infiltration between the adherends. This is confirmed by the failure mode (mainly Adhesive mode) and the fact that, although on the Ti adherend small portion of resin are visible in correspondence of the contact points with the fibres (Fig. 26a), the CFRP counterpart shows several voids between the warp-weft cross (impregnation defects), as indicate by the arrows in Fig. 26b. This limitation hinders the formation of a continuous and defect-free interphase, which is critical for effective stress transfer across the joint. As a result, the sandpaper treatment does not provide the necessary interfacial conditions to ensure high joint efficiency.

The laser cleaning treatment results in an increased surface roughness (Ra = 0.56 µm), a significantly reduced contact angle (6°), and a moderate oxide concentration (13%). These surface modifications suggest a modest increase in the apparent surface area and a substantial improvement in chemical reactivity. Furthermore, the laser-induced dimples act as micro-reservoirs for resin, facilitating superior wetting and a better mechanical interlocking between the composite and the substrate. This promotes partial fibre engagement in the failure mechanisms, as visible in Fig. 27 a-b, thereby contributing to an increase in both tensile strength and fracture energy. However, in this case also, the CFRP counterpart exhibits voids between the warp-weft intersections Fig. 27b.

However, since the matrix is neither designed to function as an adhesive nor possesses the characteristics of a structural adhesive (wettability, strength and Young's modulus), to enhance joint strength it is necessary, beyond improving chemical adhesion, increasing the effective area, enabling chemical bond formation, and to exploit the contribution of the fibres by creating effective mechanical interlocking [50,62]. The laser texturing process introduces an additional enhancement through the formation of microchannels, which exhibit two principal functions: they initiate capillary action, facilitating resin spreading across the titanium adherend, and promote mechanical interlocking with both the resin matrix and the reinforcing fibres. Capillary action is particularly pronounced in the TX1 texture, whose narrow geometry enables the utilisation of both the grooves generated by laser ablation and the intermediate channels (Fig. 28a). Moreover, this treatment appears to reduce the number of voids at the intersections of the warp and weft yarns (Fig. 28b). The anchoring mechanisms (i.e. the hooks) are mainly localised along fibres oriented parallel to the grooves, as evidenced in the cross-sectional analysis of a TX1 sample that failed in cohesive fibre (CF) mode Fig. 29. However, this does not necessarily imply the failure of fibres aligned parallel to the grooves; rather, the fibres that remain adhered to the titanium substrate are predominantly

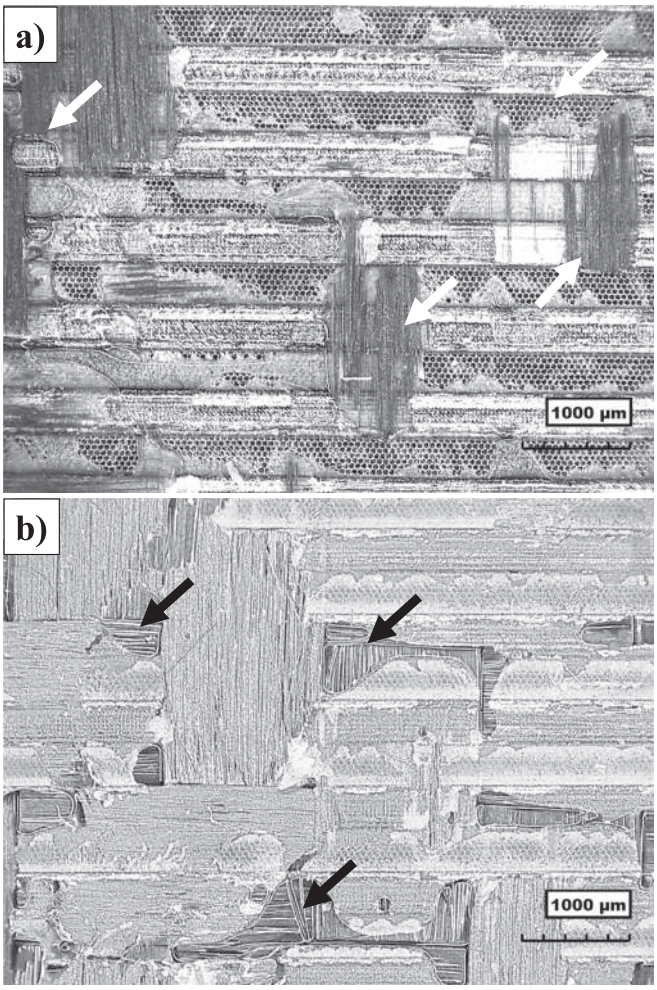

Fig. 32. Magnified view of the failure surfaces of a CTX2 sample: a) Ti side; b) CFRP side. In the figure, white and black arrows indicate fibre failure and a lack of resin, respectively.

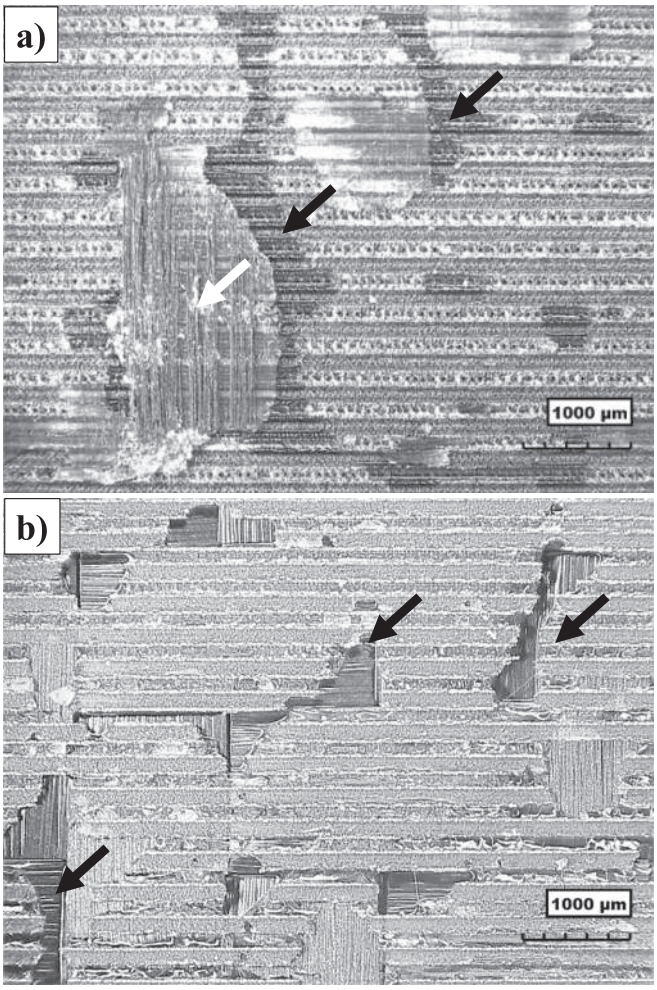

Fig. 33. Magnified view of the failure surfaces of a TX1C sample: a) Ti side; b) CFRP side. In the figure, white and black arrows indicate fibre failure and a lack of resin, respectively.

those oriented along the direction of the applied load (Fig. 28). Probably, the fractures start in correspondence with the warp and the weft cross (the black arrows in Fig. 29), where a resin excess (i.e. matrix cavity) is present and then propagates along the fibres running parallel to the loading direction, Fig. 28. Thanks to their characteristics the TX1 shows the high resistance and Failure energy (18 MPa and 23.17 J respectively). These values are comparable to those reported in the main bibliography for similar joints obtained by Secondary bonding [1,4,7,25].

Although the TX2 treatment allows a good resin spreading on the Ti surface (Fig. 30a), as confirmed by the fact that the surface imprint is well replicated on the CFRP adherend (Fig. 30b), it is unable to activate the anchoring mechanisms typical of the TX1, since: a) the grooves are larger and the taper angle is less abrupt, and b) the intermediate regions exhibit lower oxidation. Consequently, this results only in a moderate increase in strength and Failure energy (10.91 MPa and 9.39, respectively). These values are comparable to those achieved with the C treatment, which, however, requires a processing time lower by two orders of magnitude.

The adoption of laser cleaning in combination with laser texturing, since it improves the chemical bond in the area between the grooves, may contribute to increasing the joint strength. However, the effect is masked by the adopted textures. The narrow texture (CTX1) benefits from the fact that the texturing operation alone can generate the effective reinforcement mechanism (capillarity action, oxides formation and mechanical anchoring), Fig. 31. As a result, the joint strength of this treatment appears like that of the TX1 treatment. In the case of the wider texture (CTX2), microscopical inspection of the titanium surface suggests a potential improvement in adhesion, Fig. 32. However, the increase in resistance is barely visible (only comparing the average values), and it is not supported by statistically significant evidence (see Table 11, Table 12 and Fig. 19).

On the contrary, the laser cleaning post-treatment operation has a negative effect since it removes part of the oxides (TiO2) formed during the previous texturing operation, reduced the amount of recast layer produced by the prior texturing and generating a smoother surface on all the treated area, as visible in Fig. 33 and Fig. 34. This accounts for the significant reduction in joint strength observed in the samples with a narrow texture (TX1) when subjected to the laser cleaning treatment. The results obtained in this study are very encouraging and open new research lines concerning the development of surface textures that can further enhance the Ti6Al4V-CFRP Joint. Moreover, the observed increase in failure energy (up to 70 times), in line with what is reported in [41,63], suggests an improvement in fatigue resistance. However, this aspect requires an in-depth analysis and additional testing.

5. Conclusion

Various laser-based surface treatments were developed and implemented to enhance the adhesion of the hybrid Ti-CFRP joint produced by direct co-bonding. These treatments include laser texturing, laser cleaning and combinations of both laser treatments. Single lap joint tests

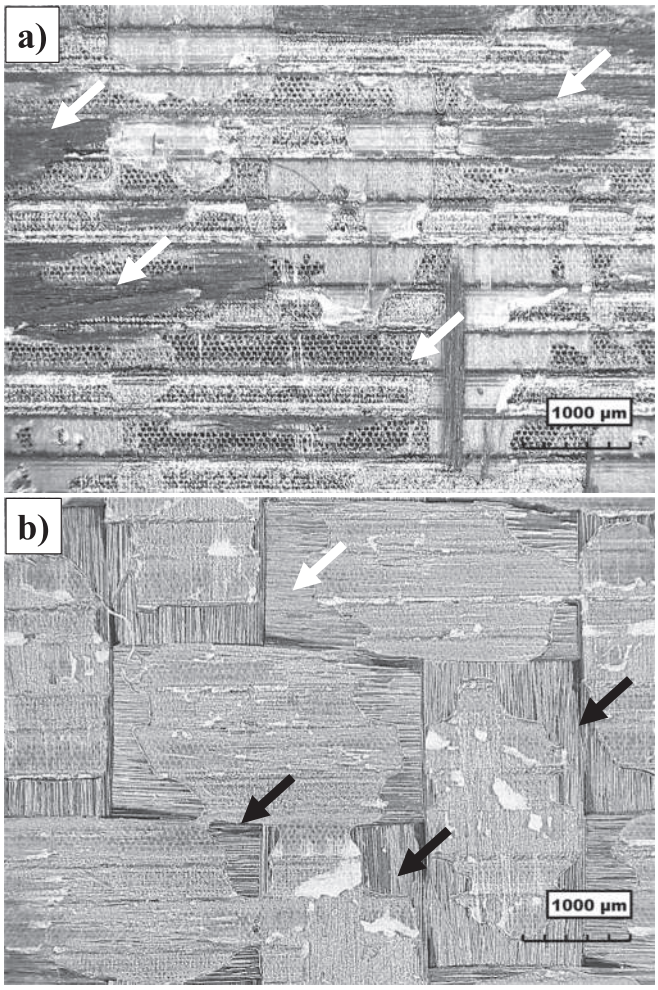

Fig. 34. Magnified view of the failure surfaces of a TX2C sample: a) Ti side; b) CFRP side. In the figure, white and black arrows indicate fibre failure and a lack of resin, respectively.

were fabricated by direct co-bonding through the resin infusion process and tested to assess the effectiveness of the treatment. Sandpaper treatment was adopted as a reference. From the results, for the adopted laser source and within the experimental conditions adopted in this work, the main conclusions are the following:

- Compared to the sandpaper treatment, laser treatments allow an increase in the joint's strength and the failure energy trough the oxide formation, the capillary action and the mechanical interlocking.
- The oxide grooving is effective when the roughness is limited, since it improves the wettability and the chemical bonding. It happens when the Ti surface is heated by the laser, as in the laser cleaning treatment alone, but not exclusively.
- Compared to the sand-paper treatment, the laser cleaning treatment allows the increase of both the joint's strength and the failure energy by 3 and 20 times (9.89 MPa and 7.48 J), respectively.
- The laser texturing treatment, in addition to producing the oxide formation and the capillarity action, allows the creation of effective mechanical interlocking mechanisms, and the fibres' contribution, resulting in a further increase of both the strength and the failure energy. These actions increase as the number of grooves (and burrs) per unit length increases and can be high enough to induce inter-laminar failure in the composite.
- Among the adopted treatments, TX1 and CTX1 give the best results both in terms of strength and failure energy (about 18 MPa and 23 J, respectively).
- These values are comparable to the ones reported in the main bibliography for similar joint configurations. Therefore, the concurrent application of laser treatment and direct co-bonding can be regarded as an efficient method for achieving effective structural bonding.

CRediT authorship contribution statement

Davide Morello: Writing – review & editing, Writing – original draft, Methodology, Investigation, Formal analysis, Data curation. **Genna Silvio:** Writing – review & editing, Resources, Methodology, Investigation, Formal analysis, Conceptualization. **Claudio Leone:** Writing – review & editing, Writing – original draft, Resources, Methodology, Investigation, Formal analysis, Data curation.

Declaration of competing interest

The authors declare that they have no known competing financial interests or personal relationships that could have appeared to influence the work reported in this paper.

Acknowledgements

The authors are particularly grateful to the Interuniversity Research Centre CIRTIBS for providing the equipment necessary to carry out the present research.

Data availability

Data will be made available on request.

References

[1] S. Li, Z. Cao, R. Chen, X. Long, C. Li, P. Li, W. Peng, Strengthening the bonding interfaces of hybrid titanium carbon laminates by bionic micro texture and carbon nanotube pinning, Compos. Sci. Technol. 232 (2023), https://doi.org/10.1016/j.compscitech.2022.109865.
[2] N. Kashaev, V. Ventzke, S. Riekehr, F. Dorn, M. Horstmann, Assessment of alternative joining techniques for Ti-6Al-4V/CFRP hybrid joints regarding tensile and fatigue strength, Mater. Des. 81 (2015) 73–81, https://doi.org/10.1016/j.matdes.2015.04.051.
[3] I. Skeist, Handbook of Adhesives (1990) 77–90, https://doi.org/10.1016/0016-0032(62)90851-7.
[4] K. Shirasu, M. Mizutani, N. Takano, H. Yoshinaga, T. Oguri, K. Ogawa, T. Okabe, S. Obayashi, Lap-shear strength and fracture behavior of CFRP/3D-printed titanium alloy adhesive joint prepared by hot-press-aided co-bonding, Int. J. Adhes. Adhes. 117 (2022), https://doi.org/10.1016/j.ijadhadh.2022.103169.
[5] H. Wang, W. Feng, Z. Zhang, Y. Guan, H. Zheng, Hybrid laser technique for joining of polymer and titanium alloy, J. Laser Appl. 31 (2019), https://doi.org/10.2351/1.5097631.
[6] P. Molitor, V. Barron, T. Young, Surface treatment of titanium for adhesive bonding to polymer composites: a review, Int. J. Adhes. Adhes. 21 (2001) 129–136, https://doi.org/10.1016/S0143-7496(00)00044-0.
[7] A.A. Khan, A.A. Al Kheraif, S.M. Alhijji, J.P. Matinlinna, Effect of grit-blasting air pressure on adhesion strength of resin to titanium, Int. J. Adhes. Adhes. 65 (2016) 41–46, https://doi.org/10.1016/j.ijadhadh.2015.11.003.
[8] C. Zhang, L. Chen, Y. Zhang, G. Wang, J. Jin, Effect of laser processing microstructure on the bonding strength and failure mode of 7075-T6 aluminum alloy adhesive joints, J. Manuf. Process. 66 (2021) 302–312, https://doi.org/10.1016/j.jmapro.2021.04.028.
[9] Z. Feng, H. Zhao, C. Tan, B. Zhu, F. Xia, Q. Wang, B. Chen, X. Song, Effect of laser texturing on the surface characteristics and bonding property of 30CrMnSiA steel adhesive joints, J. Manuf. Process. 47 (2019) 219–228, https://doi.org/10.1016/j.jmapro.2019.09.046.
[10] C. Zhang, Y. Zhang, L. Chen, Y. Chen, Effect of laser micromachining crater-array–multi-grooves on the bonding strength and failure mode of aluminum alloy adhesive joints, Opt. Laser Technol. 175 (2024) 110803, https://doi.org/10.1016/j.optlastec.2024.110803.
[11] A. Wang, A. Feng, X. Gu, X. Pan, J. Yu, Z. Jiang, Effect of picosecond laser cleaning on surface morphology and properties of stainless steel, Opt. Laser Technol. 159 (2023) 109041, https://doi.org/10.1016/j.optlastec.2022.109041.

[12] C. Leone, A. Paoletti, P. Babu Yanala, F. Lambiase, Improving bonding strength of aluminium-PEEK hybrid metal-polymer joints by two-step laser surface treatment, Opt. Laser Technol. 170 (2024) 110304, https://doi.org/10.1016/J.OPTLASTEC.2023.110304.
[13] J. Gu, X. Su, W. Li, M. Xin, D. Zhang, Y. Jin, J. Xu, B. Guo, Investigation on laser paint stripping of CFRP: Morphological evolution, damage mechanism, and adhesive performance, J. Mater. Res. Technol. 31 (2024) 3690–37021, https://doi.org/10.1016/j.jmrt.2024.07.063.
[14] M. Xu, S. Yang, X. Liu, L. Li, Y. Wan, C. Wang, M. Wu, Y. Gao, M. Zhong, B. Wang, Y. Jiang, Characterization of a two-step laser paint stripping process on CFRP, Compos. Struct. 339 (2024) 118140, https://doi.org/10.1016/j.compstruct.2024.118140.
[15] H.X. Zhang, Y.-C. Hou, Y.-F. Li, Y.-F. Yang, K. Li, J.-F. Yue, M.-Y. Jia, Y.-T. Han, Y. Yu, G. Wang, S.-P. Hou, Y.-L. Wang, Z.-W. Lu, Surface quality study of paint stripping on aircraft skins with high energy nanosecond pulsed laser cleaning, Front. Phys. 13 (2025) 1505581, https://doi.org/10.3389/fphy.2025.1505581.
[16] S. Genna, C. Leone, E. Mingione, Surface cleaning of 34CrMo4 steel pipes by using pulsed fibre laser, Int. J. Adv. Manuf. Technol. (2022), https://doi.org/10.1007/S00170-022-10648-8.
[17] V. Narayanan, R. Singh, D. Marla, Optimization of Nanosecond Pulsed Laser cleaning of Rust, Lasers Manuf. Mater. Process. 12 (2025) 68–85, https://doi.org/10.1007/s40516-025-00282-z.
[18] A. Ragusich, G. Taillon, M. Meunier, L. Martinu, J.E. Klemberg-Sapieha, Selective pulsed laser stripping of TiAlN erosion-resistant coatings: effect of wavelength and pulse duration, Surf. Coatings Technol. 232 (2013) 758–766, https://doi.org/10.1016/j.surfcoat.2013.06.092.
[19] M.P. Mateo, G. Nicolas, V. Piñon, A. Ramil, A. Yañez, Laser cleaning: an alternative method for removing oil-spill fuel residues, Appl. Surf. Sci. 247 (2005) 333–339, https://doi.org/10.1016/j.apsusc.2005.01.086.
[20] H. Li, H. Xia, L. Li, L. Li, X. Su, J. Peng, Y. Ma, C. Tan, X. Song, T. Wu, Enhancing the reliability of laser welded-brazed aluminum/stainless steel joints via laser-chemical hybrid surface texturing, Thin-Walled Struct. 199 (2024) 111780, https://doi.org/10.1016/j.tws.2024.111780.
[21] C. Coddet, G. Montavon, S. Ayrault-Costil, O. Freneaux, F. Rigolet, G. Barbezat, F. Folio, A. Diard, P. Wazen, Surface preparation and thermal spray in a single step: the PROTAL process - example of application for an aluminum-base substrate, J. Therm. Spray Technol. 8 (1999) 235–242, https://doi.org/10.1361/105996399770350467.
[22] H. Li, S. Costil, H.L. Liao, C. Coddet, Role of the laser surface preparation on the adhesion of Ni-5%Al coatings deposited using the PROTAL process, J. Therm. Spray Technol. 15 (2006) 191–197, https://doi.org/10.1361/105996306X108011.
[23] C. Mandolfino, E. Lertora, S. Genna, C. Leone, C. Gambaro, Effect of laser and plasma surface cleaning on mechanical properties of adhesive bonded joints, in, Procedia CIRP (2015) 458–463, https://doi.org/10.1016/j.procir.2015.06.054.
[24] J. Gacs, E. Sára Bogya, L. Kocsis, T. Jacob, Application of laser cleaning on AlMg4.5Mn0.4 sheets for adhesive bonding, Int. J. Adhes. Adhes. 115 (2022) 103132, https://doi.org/10.1016/j.ijadhadh.2022.103132.
[25] Z. Liu, H. Wang, Y. Chen, L. Hua, Laser-induced surface reconstruction to enhance interfacial bonding reliability of CFRP/titanium hybrid joints, J. Mater. Res. Technol. 32 (2024) 3523–3536, https://doi.org/10.1016/j.jmrt.2024.08.099.
[26] P. Maressa, L. Anodio, A. Bernasconi, A.G. Demir, B. Previtali, Effect of Surface Texture on the Adhesion Performance of Laser Treated Ti6Al4V Alloy, J. Adhes. 91 (2015) 518–537, https://doi.org/10.1080/00218464.2014.933809.
[27] C. Tan, J. Su, Z. Feng, Y. Liu, B. Chen, X. Song, Laser joining of CFRTP to titanium alloy via laser surface texturing, Chinese J. Aeronaut. 34 (2021) 103–114, https://doi.org/10.1016/j.cja.2020.08.017.
[28] Y. Liu, J. Su, C. Tan, Z. Feng, H. Zhang, L. Wu, B. Chen, X. Song, Effect of laser texturing on mechanical strength and microstructural properties of hot-pressing joining of carbon fiber reinforced plastic to Ti6Al4V, J. Manuf. Process. 65 (2021) 30–41, https://doi.org/10.1016/j.jmapro.2021.03.021.
[29] S. Liang, J. Su, H. Zhang, H. Liu, C. Tan, B. Chen, X. Song, The effect of groove texturing direction on laser joining of titanium alloy to CFRTP, Opt. Laser Technol. 171 (2024) 110416, https://doi.org/10.1016/j.optlastec.2023.110416.
[30] T.A. Schmid Fuertes, T. Kruse, T. Körwien, M. Geistbeck, Bonding of CFRP primary aerospace structures - Discussion of the certification boundary conditions and related technology fields addressing the needs for development, Compos. Interfaces 22 (2015) 795–808, https://doi.org/10.1080/09276440.2015.1077048.
[31] C. Leone, S. Genna, Effects of surface laser treatment on direct co-bonding strength of CFRP laminates, Compos. Struct. 194 (2018) 240–251, https://doi.org/10.1016/j.compstruct.2018.03.096.
[32] D. Morello, C. Leone, G. Lamanna, S. Genna, A two-step full laser surface treatment to improve the adhesive bonding of aluminium-aluminium joints, Int. J. Adhes. Adhes. 142 (2025) 104089, https://doi.org/10.1016/j.ijadhadh.2025.104089.
[33] ASTM International, ASTM D3163-01 Standard Test Method for Determining Strength of Adhesively Bonded Rigid Plastic Lap-Shear Joints in Shear by Tension Loading, (2014) 1–3.
[34] ASTM International, ASTM D5868-01 Standard Test Method for Lap Shear Adhesion for Fiber Reinforced Plastic (FRP) Bonding, (2014) 1–3.
[35] ASTM International, ASTM D1002-10 Standard Test Method for Apparent Shear Strength of Single-Lap-Joint Adhesively Bonded Metal Specimens by Tension Loading (Metal-to-Metal), (2019) 1–6.
[36] J.R. Duflou, J.W. Sutherland, D. Dornfeld, C. Herrmann, J. Jeswiet, S. Kara, M. Hauschild, K. Kellens, Towards energy and resource efficient manufacturing: a processes and systems approach, CIRP Ann. - Manuf. Technol. 61 (2012) 587–609, https://doi.org/10.1016/J.CIRP.2012.05.002.
[37] F. Apostolos, P. Alexios, P. Georgios, S. Panagiotis, C. George, Energy efficiency of manufacturing processes: a critical review, Procedia CIRP 7 (2013) 628, https://doi.org/10.1016/j.procir.2013.06.044.
[38] C. Leone, S. Genna, A. Caggiano, Resource efficient low power laser cleaning of compact discs for material reuse by polycarbonate recovery, CIRP J. Manuf. Sci. Technol. 9 (2015) 39–50, https://doi.org/10.1016/j.cirpj.2015.01.005.
[39] C. Velotti, A. Astarita, C. Leone, S. Genna, F.M.C. Minutolo, A. Squillace, Laser Marking of Titanium Coating for Aerospace applications, in, Procedia CIRP (2016) 975–980, https://doi.org/10.1016/j.procir.2016.01.006.
[40] A. Astarita, S. Genna, C. Leone, F. Memola Capece Minutolo, A. Squillace, C. Velotti, Study of the laser marking process of cold sprayed titanium coatings on aluminium substrates, Opt. Laser Technol. 83 (2016) 168–176. dOI: 10.1016/j.optlastec.2016.04.007.
[41] C. Leone, D. Morello, C. Coscione, G. Lamanna, S. Genna, A Preliminary Study on Fatigue Behavior of Aluminum Single-Lap Joints Subjected to Laser Surface Treatments, Macromol. Symp. 414 (2025) 70060, https://doi.org/10.1002/masy.70060.
[42] D.C. Montgomery, Design and Analysis of Experiments, 10th ed., Wiley, New York, NY, 2019.
[43] D.E. Coleman, D.C. Montgomery, A systematic approach to planning for a designed industrial experiment, Technometrics 53 (1993) 1–12, https://doi.org/10.1080/00401706.1993.10484984.
[44] ASTM International, ASTM D5573-99 Standard Practice for Classifying Failure Modes in Fiber-Reinforced-Plastic (FRP) Joints, (2019) 1–3.
[45] F. Lambiase, P.B. Yanala, C. Leone, A. Paoletti, Repairing aluminum-PEEK hybrid metal-polymer joints made by thermo-mechanical joining, J. Manuf. Process. 93 (2023) 1–14, https://doi.org/10.1016/J.JMAPRO.2023.03.018.
[46] J. Meijer, Laser beam machining (LBM), state of the art and new opportunities, J. Mater. Process. Technol. 149 (2004) 2–17, https://doi.org/10.1016/j.jmatprotec.2004.02.003.
[47] A. Kaldos, H.J. Pieper, E. Wolf, M. Krause, Laser machining in die making - a modern rapid tooling process, J. Mater. Process. Technol. 155–156 (2004) 1815–1820, https://doi.org/10.1016/j.jmatprotec.2004.04.258.
[48] V. Semak, A. Matsunawa, The role of recoil pressure in energy balance during laser materials processing, J. Phys. D Appl. Phys. 30 (1997) 2541–2552, https://doi.org/10.1088/0022-3727/30/18/008.
[49] F. Lambiase, P.B. Yanala, C. Leone, A. Paoletti, Influence of laser texturing strategy on thermomechanical joining of AA7075 aluminum alloy and PEEK, Compos. Struct. 315 (2023) 116974, https://doi.org/10.1016/J.COMPSTRUCT.2023.116974.
[50] R. Tao, X. Li, A. Yudhanto, M. Alfano, G. Lubineau, Laser-based interfacial patterning enables toughening of CFRP/epoxy joints through bridging of adhesive ligaments, Compos. Part A Appl. Sci. Manuf. 139 (2020) 106094, https://doi.org/10.1016/j.compositesa.2020.106094.
[51] S. Jiang, A. Zhang, X. Zhan, H. Jiang, Surface microtexturing design, laser-etching and adhesive failure of aluminum alloy single-lap-joint: Experiment and simulation, Thin-Walled Struct. 193 (2023) 111237, https://doi.org/10.1016/j.tws.2023.111237.
[52] S.M. Medjdoub, K. Madani, Y. Messid, Numerical analysis of the mechanical behavior on the effect of the geometric interface of the aluminum/aluminum plate assembly, Eurasia Proc. Sci. Technol. Eng. Math. 21 (2022) 302–310, https://doi.org/10.55549/epstem.1226626.
[53] T.C.I. 213, ISO 21920-3:2021 Geometrical product specifications (GPS) — Surface texture: Profile, (2021) 1–29.
[54] ASTM, ASTM D7334-08, Standard Practice for Surface Wettability of Coatings, Substrates and Pigments by Advancing Contact Angle Measurement, (2022) 1–3.
[55] R. Griffo, F. Di Natale, M. Minale, M. Sirignano, A. Parisi, C. Carotenuto, Analysis of Carbon Nanoparticle Coatings via Wettability, Nanomaterials 14 (2024) 301, https://doi.org/10.3390/nano14030301.
[56] J.G. Williams, C.E.M. Morris, B.C. Ennis, Liquid flow through aligned fiber beds, Polym. Eng. Sci. (1974), https://doi.org/10.1002/pen.760140603.
[57] M.P. Neupane, I.S. Park, M.H. Lee, T.S. Bae, F. Watari, Influence of heat treatment on morphological changes of nano-structured titanium oxide formed by anodic oxidation of titanium in acidic fluoride solution, Biomed. Mater. Eng. 19 (2009) 77–83, https://doi.org/10.3233/BME-2009-0566.
[58] T. Jwad, M. Walker, S. Dimov, Erasing and rewriting of titanium oxide colour marks using laser-induced reduction/oxidation, Appl. Surf. Sci. 458 (2018) 849–854, https://doi.org/10.1016/j.apsusc.2018.07.152.
[59] Y. Xue, Z. Luo, S. Han, D. Cai, H. Liu, Mechanism analysis of laser coloring of Ti alloy by optical simulation, Optik (stuttg). 254 (2022) 168650, https://doi.org/10.1016/j.ijleo.2022.168650.
[60] C.-W. Cheng, B.-S. Pasupulati, W.-T. Hsiao, Coloring of titanium by CW fiber laser irradiation and infrared temperature measurement, Opt. Commun. 528 (2023) 128983, https://doi.org/10.1016/j.optcom.2022.128983.
[61] Q. Cao, S. Zheng, C.P. Wong, S. Liu, Q. Peng, Massively Engineering the Wettability of Titanium by Tuning Nanostructures and Roughness via Laser Ablation, J. Phys. Chem. C 123 (2019) 30382–30388, https://doi.org/10.1021/acs.jpcc.9b08580.
[62] T. Bagnato, A.R. Ravindran, A. Mirabedini, R.B. Ladani, E. Kandare, A.C. Orifici, P. Chang, J. Wang, A.P. Mouritz, Superior interfacial toughening of hybrid metal-composite structural joints using 3D printed pins, Compos. Part A Appl. Sci. Manuf. 168 (2023) 107479, https://doi.org/10.1016/j.compositesa.2023.107479.
[63] F. Moroni, F. Musiari, C. Favi, Effect of the surface morphology over the fatigue performance of metallic single lap-shear joints, Int. J. Adhes. Adhes. 97 (2020) 102484, https://doi.org/10.1016/j.ijadhadh.2019.102484.